

# Local Porosity Theory and Stochastic Reconstruction for Porous Media

Rudolf Hilfer

ICA-1, Universität Stuttgart, 70569 Stuttgart, Germany  
Institut für Physik, Universität Mainz, 55099 Mainz, Germany

**Abstract.** The paper reviews recent developments in local porosity theory, and discusses its application to the analysis of stochastic reconstruction models for sedimentary rocks. Special emphasis is placed on the geometric observables in local porosity theory and their relation with the Hadwiger theorem from stochastic geometry. In addition recent results for the exact calculation of effective physical transport properties are given for a Fontainebleau sandstone. The calculations pertain to potential type problems such as electrical conduction, dielectric relaxation, diffusion or Darcy flow. The exact results are compared to the approximate parameterfree predictions from local porosity, and are found to be in good agreement.

## 1 Introduction

An important subclass of heterogeneous and disordered systems are porous materials which can be loosely defined as mixtures of solids and fluids [1,20,30,55]. Despite a long history of scientific study the theory of porous media or, more generally, heterogeneous mixtures (including solid-solid and fluid-fluid mixtures) continues to be of central interest for many areas of fundamental and applied research ranging from geophysics [26], hydrology [7,43], petrophysics [36] and civil engineering [19,21] to the materials science of composites [17].

My primary objective in this article is to review briefly the application of local porosity theory, introduced in [27,28,30], to the geometric characterization of porous or heterogeneous media. A functional theorem of Hadwiger [23, p.39] emphasizes the importance of four set-theoretic functionals for the geometric characterization porous media (see also the paper by Mecke in this volume). In contrast herewith local porosity theory has emphasized geometric observables, that are not covered by Hadwigers theorem [25,29,31]. Other theories have stressed the importance of correlation functions [60,63] or contact distributions [38,46,61] for characterization purposes. Recently advances in computer and imaging technology have made threedimensional microtomographic images more readily available. Exact microscopic solutions are thereby becoming possible and have recently been calculated [11,66,68]. Moreover, the availability of threedimensional microstructures allows to test approximate theories and geometric models and to distinguish them quantitatively.

Distinguishing porous microstructures in a quantitative fashion is important for reliable predictions and it requires apt geometric observables. Examples of important geometric observables are porosity and specific internal surface area

[6,20]. It is clear however, that porosity and specific internal surface area alone are not sufficient to distinguish the infinite variety of porous microstructures.

Geometrical models for porous media may be roughly subdivided into the classical capillary tube and slit models [6], grain models [61], network models [15,22], percolation models [16,54], fractal models [34,53], stochastic reconstruction models [1,49] and diagenetic models [4,51]. Little attention is usually paid to match the geometric characteristics of a model geometry to those of the experimental sample, as witnessed by the undiminished popularity of capillary tube models. Usually the matching of geometric observables is limited to the porosity alone. Recently the idea of stochastic reconstruction models has found renewed interest [1,50,70]. In stochastic reconstruction models one tries to match not only the porosity but also other geometric quantities such as specific internal surface, correlation functions, or linear and spherical contact distributions. Similar ideas have been proposed in spatial statistics [61]. As the number of matched quantities increases one expects that also the model approximates better the given sample. My secondary objective in this review will be to compare simple stochastic reconstruction models and physically inspired diagenesis models with the experimental microstructure obtained from computer tomography [11].

## 2 Problems in the Theory of Porous Media

### 2.1 Physical Problems

Many physical problems in porous and heterogeneous media can be formulated mathematically as a set of partial differential equations

$$\mathbf{F}_{\mathbb{P}}(\mathbf{r}, t, \mathbf{u}, \partial\mathbf{u}/\partial t, \dots, \nabla \cdot \mathbf{u}, \nabla \times \mathbf{u}, \dots) = 0, \quad \mathbf{r} \in \mathbb{P} \subset \mathbb{R}^3, t \in \mathbb{R} \quad (1a)$$

$$\mathbf{F}_{\mathbb{M}}(\mathbf{r}, t, \mathbf{u}, \partial\mathbf{u}/\partial t, \dots, \nabla \cdot \mathbf{u}, \nabla \times \mathbf{u}, \dots) = 0, \quad \mathbf{r} \in \mathbb{M} \subset \mathbb{R}^3, t \in \mathbb{R} \quad (1b)$$

for a vector of unknown fields  $\mathbf{u}(\mathbf{r}, t)$  as function of position and time coordinates. Here the two-component porous sample  $\mathbb{S} = \mathbb{P} \cup \mathbb{M}$  is defined as the union of two closed subsets  $\mathbb{P} \subset \mathbb{R}^3$  and  $\mathbb{M} \subset \mathbb{R}^3$  where  $\mathbb{P}$  denotes the pore space (or component 1 in a heterogeneous medium) and  $\mathbb{M}$  denotes the matrix space (or component 2). In (1) the vector functionals  $\mathbf{F}_{\mathbb{P}}$  and  $\mathbf{F}_{\mathbb{M}}$  may depend on the vector  $\mathbf{u}$  of unknowns and its derivatives as well as on position  $\mathbf{r}$  and time  $t$ . A simple example for (1) is the time independent potential problem

$$\nabla \cdot \mathbf{j}(\mathbf{r}) = 0, \quad \mathbf{r} \in \mathbb{S} \quad (2)$$

$$\mathbf{j}(\mathbf{r}) + C(\mathbf{r})\nabla u(\mathbf{r}) = 0, \quad \mathbf{r} \in \mathbb{S} \quad (3)$$

for a scalar field  $u(\mathbf{r})$ . The coefficients

$$C(\mathbf{r}) = C_{\mathbb{P}}\chi_{\mathbb{P}}(\mathbf{r}) + C_{\mathbb{M}}\chi_{\mathbb{M}}(\mathbf{r}) \quad (4)$$

contain the material constants  $C_{\mathbb{P}} \neq C_{\mathbb{M}}$ . Here the characteristic (or indicator) function  $\chi_{\mathbb{G}}(\mathbf{r})$  of a set  $\mathbb{G}$  is defined as

$$\chi_{\mathbb{G}}(\mathbf{r}) = \begin{cases} 1 & \text{for } \mathbf{r} \in \mathbb{G} \\ 0 & \text{for } \mathbf{r} \notin \mathbb{G}. \end{cases} \quad (5)$$

Hence  $C(\mathbf{r})$  is not differentiable at the internal boundary  $\partial_{\mathbb{P}} = \partial_{\mathbb{M}}$ , and this requires to specify boundary conditions

$$\lim_{\mathbf{s} \rightarrow \mathbf{r}} \mathbf{n} \cdot \mathbf{j}(\mathbf{r} + \mathbf{s}) = \lim_{\mathbf{s} \rightarrow \mathbf{r}} \mathbf{n} \cdot \mathbf{j}(\mathbf{r} - \mathbf{s}), \quad \mathbf{r} \in \partial \mathbb{P} \quad (6)$$

$$\lim_{\mathbf{s} \rightarrow \mathbf{r}} \mathbf{n} \times \nabla u(\mathbf{r} + \mathbf{s}) = \lim_{\mathbf{s} \rightarrow \mathbf{r}} \mathbf{n} \times \nabla u(\mathbf{r} - \mathbf{s}), \quad \mathbf{r} \in \partial \mathbb{P} \quad (7)$$

at the internal boundary. In addition, boundary conditions on the sample boundary  $\partial \mathbb{S}$  need to be given to complete the formulation of the problem. Initial conditions may also be required. Several concrete applications can be subsumed under this formulation depending upon the physical interpretation of the field  $u$  and the current  $\mathbf{j}$ . An overview for possible interpretations of  $u$  and  $\mathbf{j}$  is given in Table 2.1. It contains hydrodynamical flow, electrical conduction, heat conduction and diffusion as well as cross effects such as thermoelectric or electrokinetic phenomena.

**Table 1.** Overview of possible interpretations for the field  $u$  and the current  $\mathbf{j}$  produced by its gradient according to (3).

$\mathbf{j} \setminus u$	pressure	el. potential	temperature	concentration
volume	Darcy's law	electroosmosis	thermal osmosis	chemical osmosis
el. charge	streaming pot.	Ohm's law	Seebeck effect	sedim. electricity
heat	thermal filtration	Peltier effect	Fourier's law	Dufour effect
particles	ultrafiltration	electrophoresis	Soret effect	Fick's law

The physical problems in the theory of porous media may be divided into two categories: direct problems and inverse problems. In direct problems one is given partial information about the pore space configuration  $\mathbb{P}$ . The problem is to deduce information about the solution  $u(\mathbf{r}, t)$  of the boundary and/or initial value problem that can be compared to experiment. In inverse problems one is given partial information about the solutions  $u(\mathbf{r}, t)$ . Typically this information comes from various experiments or observations of physical processes. The problem is to deduce information about the pore space configuration  $\mathbb{P}$  from these data.

Inverse problems are those of greatest practical interest. All attempts to visualize the internal interface or fluid content of nontransparent heterogeneous media lead to inverse problems. Examples occur in computer tomography. Inverse problems are often ill-posed due to lack of data [39,52]. Reliable solution of inverse problems requires a predictive theory for the direct problem.

## 2.2 Geometrical Problems

The geometrical problems arise because in practice the pore space configuration  $\chi_{\mathbb{P}}(\mathbf{r})$  is usually not known in detail. The direct problem, i.e. the solution of a physical boundary value problem, requires detailed knowledge of the internal boundary, and hence of  $\chi_{\mathbb{P}}(\mathbf{r})$ .

While it is becoming feasible to digitize samples of several  $\text{mm}^3$  with a resolution of a few  $\mu\text{m}$  this is not possible for larger samples. For this reason the true pore space  $\mathbb{P}$  is often replaced by a geometric model  $\tilde{\mathbb{P}}$ . One then solves the problem for the model geometry and hopes that its solution  $\tilde{u}$  obeys  $\tilde{u} \approx u$  in some sense. Such an approach requires quantitative methods for the comparison of  $\mathbb{P}$  and the model  $\tilde{\mathbb{P}}$ . This raises the problem of finding generally applicable quantitative geometric characterization methods that allow to evaluate the accuracy of geometric models for porous microstructures. The problem of quantitative geometric characterization arises also when one asks which geometrical characteristics of the microstructure  $\mathbb{P}$  have the greatest influence on the properties of the solution  $u$  of a given boundary value problem.

Some authors introduce more than one geometrical model for one and the same microstructure when calculating different physical properties (e.g. diffusion and conduction). It should be clear that such models make it difficult to extract reliable physical or geometrical information.

### 3 Geometric Characterizations

#### 3.1 General Considerations

A general geometric characterization of stochastic media should provide macroscopic geometric observables that allow to distinguish media with different microstructures quantitatively. In general, a stochastic medium is defined as a probability distribution on a space of geometries or configurations. Distributions and expectation values of geometric observables are candidates for a general geometric characterization.

A general geometric characterization should fulfill four criteria to be useful in applications. These four criteria were advanced in [30]. First, it must be well defined. This obvious requirement is sometimes violated. The so called “pore size distributions” measured in mercury porosimetry are not geometrical observables in the sense that they cannot be determined from knowledge of the geometry alone. Instead they are capillary pressure curves whose calculation involves physical quantities such as surface tension, viscosity or flooding history [30]. Second, the geometric characterization should be directly accessible in experiments. The experiments should be independent of the quantities to be predicted. Thirdly, the numerical implementation should not require excessive amounts of data. This means that the amount of data should be manageable by contemporary data processing technology. Finally, a useful geometric characterization should be helpful in the exact or approximate theoretical calculations.

For simplicity only two-component media will be considered throughout this paper, but most concepts can be generalized to media with an arbitrary finite number of components.

#### 3.2 Geometric Observables

Well defined geometric observables are the basis for the geometric characterization of porous media. A perennial problem in all applications is to identify those

macroscopic geometric observables that are relevant for distinguishing between classes of microstructures. One is interested in those properties of the microstructure that influence the macroscopic physical behaviour. In general this depends on the details of the physical problem, but some general properties of the microstructure such as volume fraction or porosity are known to be relevant in many situations. Hadwiger's theorem [23] is an example of a mathematical result that helps to identify an important class of such general geometric properties of porous media. It will be seen later, however, that there exist important geometric properties that are not members of this class.

A two component porous (or heterogenous) sample  $\mathbb{S} \subset \mathbb{R}^d$  consists of two closed subsets  $\mathbb{P} \subset \mathbb{R}^d$  and  $\mathbb{M} \subset \mathbb{R}^d$  called pore space  $\mathbb{P}$  and matrix  $\mathbb{M}$  such that  $\mathbb{S} = \mathbb{P} \cup \mathbb{M}$ . Its internal boundary is denoted as  $\partial\mathbb{P} = \partial\mathbb{M} = \mathbb{P} \cap \mathbb{M}$ . The boundary  $\partial\mathbb{G}$  of a set is defined as the difference between the closure and the interior of  $\mathbb{G}$  where the closure is the intersection of all closed sets containing  $\mathbb{G}$  and the interior is the union of all open sets contained in  $\mathbb{G}$ . A geometric observable  $f$  is a mapping (functional) that assigns to each admissible  $\mathbb{P}$  a real number  $f(\mathbb{P}) = f(\mathbb{P} \cap \mathbb{S})$  that can be calculated from  $\mathbb{P}$  without solving a physical boundary value problem. A functional whose evaluation requires the solution of a physical boundary value problem will be called a physical observable.

Before discussing examples for geometric observables it is necessary to specify the admissible geometries  $\mathbb{P}$ . The set  $\mathcal{R}$  of admissible  $\mathbb{P}$  is defined as the set of all finite unions of compact convex sets [23,44,57,58,61] (see also the papers by M. Kerscher and K. Mecke in this volume). Because  $\mathcal{R}$  is closed under unions and intersections it is called the convex ring. The choice of  $\mathcal{R}$  is convenient for applications because digitized porous media can be considered as elements from  $\mathcal{R}$  and because continuous observables defined for convex compact sets can be continued to all of  $\mathcal{R}$ . The set of all compact and convex subsets of  $\mathbb{R}^d$  is denoted as  $\mathcal{K}$ . For subsequent discussions the Minkowski addition of two sets  $\mathbb{A}, \mathbb{B} \subset \mathbb{R}^d$  is defined as

$$\mathbb{A} + \mathbb{B} = \{\mathbf{x} + \mathbf{y} : \mathbf{x} \in \mathbb{A}, \mathbf{y} \in \mathbb{B}\}. \tag{8}$$

Multiplication of  $\mathbb{A}$  with a scalar is defined by  $a\mathbb{A} = \{a\mathbf{x} : \mathbf{x} \in \mathbb{A}\}$  for  $a \in \mathbb{R}$ .

Examples of geometric observables are the volume of  $\mathbb{P}$  or the surface area of its boundary  $\partial\mathbb{P}$ . Let

$$V_d(\mathbb{K}) = \int_{\mathbb{R}^d} \chi_{\mathbb{P}}(\mathbf{r}) d^d \mathbf{r} \tag{9}$$

denote the  $d$ -dimensional Lebesgue volume of the compact convex set  $\mathbb{K}$ . The volume is hence a functional  $V_d : \mathcal{K} \rightarrow \mathbb{R}$  on  $\mathcal{K}$ . An example of a compact convex set is the unit ball  $\mathbb{B}^d = \{\mathbf{x} \in \mathbb{R}^d : |\mathbf{x}| \leq 1\} = \mathbb{B}^d(\mathbf{0}, 1)$  centered at the origin  $\mathbf{0}$  whose volume is

$$\kappa_d = V_d(\mathbb{B}^d) = \frac{\pi^{d/2}}{\Gamma(1 + (d/2))}. \tag{10}$$

Other functionals on  $\mathcal{K}$  can be constructed from the volume by virtue of the following fact. For every compact convex  $\mathbb{K} \in \mathcal{K}$  and every  $\varepsilon \geq 0$  there are

numbers  $V_j(\mathbb{K}), j = 0, \dots, d$  depending only on  $\mathbb{K}$  such that

$$V_d(\mathbb{K} + \varepsilon\mathbb{B}^d) = \sum_{j=0}^d V_j(\mathbb{K})\varepsilon^{d-j}\kappa_{d-j} \tag{11}$$

is a polynomial in  $\varepsilon$ . This result is known as Steiners formula [23,61]. The numbers  $V_j(\mathbb{K}), j = 0 \dots, d$  define functionals on  $\mathcal{K}$  similar to the volume  $V_d(\mathbb{K})$ . The quantities

$$W_i(\mathbb{K}) = \frac{\kappa_i V_{d-i}(\mathbb{K})}{\binom{d}{i}} \tag{12}$$

are called quermassintegrals [57]. From (11) one sees that

$$\lim_{\varepsilon \rightarrow 0} \frac{1}{\varepsilon} (V_d(\mathbb{K} + \varepsilon\mathbb{B}^d) - V_d(\mathbb{K})) = \kappa_1 V_{d-1}(\mathbb{K}), \tag{13}$$

and from (10) that  $\kappa_1 = 2$ . Hence  $V_{d-1}(\mathbb{K})$  may be viewed as half the surface area. The functional  $V_1(\mathbb{K})$  is related to the mean width  $w(\mathbb{K})$  defined as the mean value of the distance between a pair of parallel support planes of  $\mathbb{K}$ . The relation is

$$V_1(\mathbb{K}) = \frac{d\kappa_d}{2\kappa_{d-1}} w(\mathbb{K}) \tag{14}$$

which reduces to  $V_1(\mathbb{K}) = w(\mathbb{K})/2$  for  $d = 3$ . Finally the functional  $V_0(\mathbb{K})$  is evaluated from (11) by dividing with  $\varepsilon^d$  and taking the limit  $\varepsilon \rightarrow \infty$ . It follows that  $V_0(\mathbb{K}) = 1$  for all  $\mathbb{K} \in \mathcal{K} \setminus \{\emptyset\}$ . One extends  $V_0$  to all of  $\mathcal{K}$  by defining  $V_0(\emptyset) = 0$ . The geometric observable  $V_0$  is called Euler characteristic.

The geometric observables  $V_i$  have several important properties. They are Euclidean invariant (i.e. invariant under rigid motions), additive and monotone. Let  $T_d \cong (\mathbb{R}^d, +)$  denote the group of translations with vector addition as group operation and let  $SO(d)$  be the matrix group of rotations in  $d$  dimensions [5]. The semidirect product  $E_d = T_d \odot SO(d)$  is the Euclidean group of rigid motions in  $\mathbb{R}^d$ . It is defined as the set of pairs  $(\mathbf{a}, A)$  with  $\mathbf{a} \in T_d$  and  $A \in SO(d)$  and group operation

$$(\mathbf{a}, A) \circ (\mathbf{b}, B) = (\mathbf{a} + A\mathbf{b}, AB). \tag{15}$$

An observable  $f : \mathcal{K} \rightarrow \mathbb{R}$  is called euclidean invariant or invariant under rigid motions if

$$f(\mathbf{a} + A\mathbb{K}) = f(\mathbb{K}) \tag{16}$$

holds for all  $(\mathbf{a}, A) \in E_d$  and all  $\mathbb{K} \in \mathcal{K}$ . Here  $A\mathbb{K} = \{A\mathbf{x} : \mathbf{x} \in \mathbb{K}\}$  denotes the rotation of  $\mathbb{K}$  and  $\mathbf{a} + \mathbb{K} = \{\mathbf{a}\} + \mathbb{K}$  its translation. A geometric observable  $f$  is called additive if

$$f(\emptyset) = 0 \tag{17a}$$

$$f(\mathbb{K}_1 \cup \mathbb{K}_2) + f(\mathbb{K}_1 \cap \mathbb{K}_2) = f(\mathbb{K}_1) + f(\mathbb{K}_2) \tag{17b}$$

holds for all  $\mathbb{K}_1, \mathbb{K}_2 \in \mathcal{K}$  with  $\mathbb{K}_1 \cup \mathbb{K}_2 \in \mathcal{K}$ . Finally a functional is called monotone if for  $\mathbb{K}_1, \mathbb{K}_2 \in \mathcal{K}$  with  $\mathbb{K}_1 \subset \mathbb{K}_2$  follows  $f(\mathbb{K}_1) \leq f(\mathbb{K}_2)$ .

The special importance of the functionals  $V_i(\mathbb{K})$  arises from the following theorem of Hadwiger [23]. A functional  $f : \mathcal{K} \rightarrow \mathbb{R}$  is euclidean invariant, additive and monotone if and only if it is a linear combination

$$f = \sum_{i=0}^d c_i V_i \tag{18}$$

with nonnegative constants  $c_0, \dots, c_d$ . The condition of monotonicity can be replaced with continuity and the theorem remains valid [23]. If  $f$  is continuous on  $\mathcal{K}$ , additive and euclidean invariant it can be additively extended to the convex ring  $\mathcal{R}$  [58]. The additive extension is unique and given by the inclusion-exclusion formula

$$f \left( \bigcup_{i=1}^m \mathbb{K}_i \right) = \sum_{\mathbb{I} \in \mathcal{P}(m)} (-1)^{|\mathbb{I}|-1} f \left( \bigcap_{i \in \mathbb{I}} \mathbb{K}_i \right) \tag{19}$$

where  $\mathcal{P}(m)$  denotes the family of nonempty subsets of  $\{1, \dots, m\}$  and  $|\mathbb{I}|$  is the number of elements of  $\mathbb{I} \in \mathcal{P}(m)$ . In particular, the functionals  $V_i$  have a unique additive extension to the convex ring  $\mathcal{R}$  [58], which is again denoted by  $V_i$ .

For a threedimensional porous sample with  $\mathbb{P} \in \mathcal{R}$  the extended functionals  $V_i$  lead to two frequently used geometric observables. The first is the porosity of a porous sample  $\mathbb{S}$  defined as

$$\phi(\mathbb{P} \cap \mathbb{S}) = \phi_3(\mathbb{P} \cap \mathbb{S}) = \frac{V_3(\mathbb{P} \cap \mathbb{S})}{V_3(\mathbb{S})}, \tag{20}$$

and the second its specific internal surface area which may be defined in view of (13) as

$$\phi_2(\mathbb{P} \cap \mathbb{S}) = \frac{2V_2(\mathbb{P} \cap \mathbb{S})}{V_3(\mathbb{S})}. \tag{21}$$

The two remaining observables  $\phi_1(\mathbb{P}) = V_1(\mathbb{P} \cap \mathbb{S})/V_3(\mathbb{S})$  and  $\phi_0(\mathbb{P}) = V_0(\mathbb{P} \cap \mathbb{S})/V_3(\mathbb{S})$  have received less attention in the porous media literature. The Euler characteristic  $V_0$  on  $\mathcal{R}$  coincides with the identically named topological invariant. For  $d = 2$  and  $\mathbb{G} \in \mathcal{R}$  one has  $V_0(\mathbb{G}) = c(\mathbb{G}) - c'(\mathbb{G})$  where  $c(\mathbb{G})$  is the number of connectedness components of  $\mathbb{G}$ , and  $c'(\mathbb{G})$  denotes the number of holes (i.e. bounded connectedness components of the complement).

### 3.3 Definition of Stochastic Porous Media

For theoretical purposes the pore space  $\mathbb{P}$  is frequently viewed as a random set [30,61]. In practical applications the pore space is usually discretized because of measurement limitations and finite resolution. For the data discussed below the set  $\mathbb{S} \subset \mathbb{R}^3$  is a rectangular parallelepiped whose sidelengths are  $M_1, M_2$  and  $M_3$  in units of the lattice constant  $a$  (resolution) of a simple cubic lattice. The position vectors  $\mathbf{r}_i = \mathbf{r}_{i_1 \dots i_d} = (ai_1, \dots, ai_d)$  with integers  $1 \leq i_j \leq M_j$  are

used to label the lattice points, and  $\mathbf{r}_i$  is a shorthand notation for  $\mathbf{r}_{i_1 \dots i_d}$ . Let  $\mathbb{V}_i$  denote a cubic volume element (voxel) centered at the lattice site  $\mathbf{r}_i$ . Then the discretized sample may be represented as  $\mathbb{S} = \bigcup_{i=1}^N \mathbb{V}_i$ . The discretized pore space  $\tilde{\mathbb{P}}$  defined as

$$\tilde{\mathbb{P}} = \bigcup_{\{i: \chi_{\mathbb{P}}(\mathbf{r}_i)=1\}} \mathbb{V}_i. \quad (22)$$

is an approximation to the true pore space  $\mathbb{P}$ . For simplicity it will be assumed that the discretization does not introduce errors, i.e. that  $\tilde{\mathbb{P}} = \mathbb{P}$ , and that each voxel is either fully pore or fully matrix. This assumption may be relaxed to allow voxel attributes such as internal surface or other quermassintegral densities. The discretization into voxels reflects the limitations arising from the experimental resolution of the porous structure. A discretized pore space for a bounded sample belongs to the convex ring  $\mathcal{R}$  if the voxels are convex and compact. Hence, for a simple cubic discretization the pore space belongs to the convex ring. A configuration (or microstructure)  $\mathbf{Z}$  of a 2-component medium may then be represented in the simplest case by a sequence

$$\mathbf{Z} = (Z_1, \dots, Z_N) = (\chi_{\mathbb{P}}(\mathbf{r}_1), \dots, \chi_{\mathbb{P}}(\mathbf{r}_N)) \quad (23)$$

where  $\mathbf{r}_i$  runs through the lattice points and  $N = M_1 M_2 M_3$ . This representation corresponds to the simplest discretization in which there are only two states for each voxel indicating whether it belongs to pore space or not. In general a voxel could be characterized by more states reflecting the microstructure within the region  $\mathbb{V}_i$ . In the simplest case there is a one-to-one correspondence between  $\mathbb{P}$  and  $\mathbf{Z}$  given by (23). Geometric observables  $f(\mathbb{P})$  then correspond to functions  $f(\mathbf{Z}) = f(z_1, \dots, z_N)$ .

As a convenient theoretical idealization it is frequently assumed that porous media are random realizations drawn from an underlying statistical ensemble. A discretized stochastic porous medium is defined through the discrete probability density

$$p(z_1, \dots, z_N) = \text{Prob}\{(Z_1 = z_1) \wedge \dots \wedge (Z_N = z_N)\} \quad (24)$$

where  $z_i \in \{0, 1\}$  in the simplest case. It should be emphasized that the probability density  $p$  is mainly of theoretical interest. In practice it is usually not known. An infinitely extended medium or microstructure is called stationary or statistically homogeneous if  $p$  is invariant under spatial translations. It is called isotropic if  $p$  is invariant under rotations.

### 3.4 Moment Functions and Correlation Functions

A stochastic medium was defined through its probability distribution  $p$ . In practice  $p$  will be even less accessible than the microstructure  $\mathbb{P} = \mathbf{Z}$  itself. Partial information about  $p$  can be obtained by measuring or calculating expectation values of a geometric observable  $f$ . These are defined as

$$\langle f(z_1, \dots, z_N) \rangle = \sum_{z_1=0}^1 \dots \sum_{z_N=0}^1 f(z_1, \dots, z_N) p(z_1, \dots, z_N) \quad (25)$$

where the summations indicate a summation over all configurations. Consider for example the porosity  $\phi(\mathbb{S})$  defined in (20). For a stochastic medium  $\phi(\mathbb{S})$  becomes a random variable. Its expectation is

$$\begin{aligned} \langle \phi \rangle &= \frac{\langle V_3(\mathbb{P}) \rangle}{V_3(\mathbb{S})} = \frac{1}{V_3(\mathbb{S})} \int_{\mathbb{S}} \langle \chi_{\mathbb{P}}(\mathbf{r}) \rangle d^3\mathbf{r} \\ &= \frac{1}{V_3(\mathbb{S})} \sum_{i=1}^N \langle z_i \rangle V_3(\mathbb{V}_i) = \frac{1}{N} \sum_{i=1}^N \langle z_i \rangle \\ &= \frac{1}{N} \sum_{i=1}^N \text{Prob}\{z_i = 1\} = \frac{1}{N} \sum_{i=1}^N \text{Prob}\{\mathbf{r}_i \in \mathbb{P}\} \end{aligned} \quad (26)$$

If the medium is statistically homogeneous then

$$\langle \phi \rangle = \text{Prob}\{z_i = 1\} = \text{Prob}\{\mathbf{r}_i \in \mathbb{P}\} = \langle \chi_{\mathbb{P}}(\mathbf{r}_i) \rangle \quad (27)$$

independent of  $i$ . It happens frequently that one is given only a single sample, not an ensemble of samples. It is then necessary to invoke an ergodic hypothesis that allows to equate spatial averages with ensemble averages.

The porosity is the first member in a hierarchy of moment functions. The  $n$ -th order moment function is defined generally as

$$S_n(\mathbf{r}_1, \dots, \mathbf{r}_n) = \langle \chi_{\mathbb{P}}(\mathbf{r}_1) \dots \chi_{\mathbb{P}}(\mathbf{r}_n) \rangle \quad (28)$$

for  $n \leq N$ . (If a voxel has other attributes besides being pore or matrix one may define also mixed moment functions  $S_{i_1 \dots i_n}(\mathbf{r}_1, \dots, \mathbf{r}_n) = \langle \phi_{i_1}(\mathbf{r}_1) \dots \phi_{i_n}(\mathbf{r}_n) \rangle$  where  $\phi_i(\mathbf{r}_j) = V_i(\mathbb{P} \cap \mathbb{V}_j)/V_i(\mathbb{V}_j)$  for  $i = 1, \dots, d$  are the quermassintegral densities for the voxel at site  $\mathbf{r}_j$ .) For stationary media  $S_n(\mathbf{r}_1, \dots, \mathbf{r}_n) = g(\mathbf{r}_1 - \mathbf{r}_n, \dots, \mathbf{r}_{n-1} - \mathbf{r}_n)$  where the function  $g$  depends only on  $n-1$  variables. Another frequently used expectation value is the correlation function which is related to  $S_2$ . For a homogeneous medium it is defined as

$$G(\mathbf{r}_0, \mathbf{r}) = G(\mathbf{r} - \mathbf{r}_0) = \frac{\langle \chi_{\mathbb{P}}(\mathbf{r}_0) \chi_{\mathbb{P}}(\mathbf{r}) \rangle - \langle \phi \rangle^2}{\langle \phi \rangle (1 - \langle \phi \rangle)} = \frac{S_2(\mathbf{r} - \mathbf{r}_0) - (S_1(\mathbf{r}_0))^2}{S_1(\mathbf{r}_0)(1 - S_1(\mathbf{r}_0))} \quad (29)$$

where  $\mathbf{r}_0$  is an arbitrary reference point, and  $\langle \phi \rangle = S_1(\mathbf{r}_0)$ . If the medium is isotropic then  $G(\mathbf{r}) = G(|\mathbf{r}|) = G(r)$ . Note that  $G$  is normalized such that  $G(0) = 1$  and  $G(\infty) = 0$ .

The hierarchy of moment functions  $S_n$ , similar to  $p$ , is mainly of theoretical interest. For a homogeneous medium  $S_n$  is a function of  $n-1$  variables. To specify  $S_n$  numerically becomes impractical as  $n$  increases. If only 100 points are required along each coordinate axis then giving  $S_n$  would require  $10^{2d(n-1)}$  numbers. For  $d = 3$  this implies that already at  $n = 3$  it becomes economical to specify the microstructure  $\mathbb{P}$  directly rather than incompletely through moment or correlation functions.

### 3.5 Contact Distributions

An interesting geometric characteristic introduced and discussed in the field of stochastic geometry are contact distributions [18,61, p. 206]. Certain special cases of contact distributions have appeared also in the porous media literature [20]. Let  $\mathbb{G}$  be a compact test set containing the origin  $\mathbf{0}$ . Then the contact distribution is defined as the conditional probability

$$H_{\mathbb{G}}(r) = 1 - \text{Prob}\{\mathbf{0} \notin \mathbb{M} + (-r\mathbb{G}) | \mathbf{0} \notin \mathbb{M}\} = 1 - \frac{\text{Prob}\{\mathbb{M} \cap r\mathbb{G} = \emptyset\}}{\phi} \quad (30)$$

If one defines the random variable  $R = \inf\{s : \mathbb{M} \cap s\mathbb{G} \neq \emptyset\}$  then  $H_{\mathbb{G}}(r) = \text{Prob}\{R \leq r | R > 0\}$  [61].

For the unit ball  $\mathbb{G} = \mathbb{B}(\mathbf{0}, 1)$  in three dimensions  $H_{\mathbb{B}}$  is called spherical contact distribution. The quantity  $1 - H_{\mathbb{B}}(r)$  is then the distribution function of the random distance from a randomly chosen point in  $\mathbb{P}$  to its nearest neighbour in  $\mathbb{M}$ . The probability density

$$p(r) = \frac{d}{dr}(1 - H_{\mathbb{B}}(r)) = -\frac{d}{dr}H_{\mathbb{B}}(r) \quad (31)$$

was discussed in [56] as a well defined alternative to the frequently used pore size distribution from mercury porosimetry.

For an oriented unit interval  $\mathbb{G} = \mathbb{B}^1(\mathbf{0}, 1; \mathbf{e})$  where  $\mathbf{e}$  is the a unit vector one obtains the linear contact distribution. The linear contact distribution written as  $L(r\mathbf{e}) = \phi(1 - H_{\mathbb{B}^1(\mathbf{0}, 1; \mathbf{e})}(r))$  is sometimes called lineal path function [70]. It is related to the chord length distribution  $p_{cl}(x)$  defined as the probability that an interval in the intersection of  $\mathbb{P}$  with a straight line containing  $\mathbb{B}^1(\mathbf{0}, 1; \mathbf{e})$  has length smaller than  $x$  [30,61, p. 208].

### 3.6 Local Porosity Distributions

The idea of local porosity distributions is to measure geometric observables inside compact convex subsets  $\mathbb{K} \subset \mathbb{S}$ , and to collect the results into empirical histograms [27]. Let  $\mathbb{K}(\mathbf{r}, L)$  denote a cube of side length  $L$  centered at the lattice vector  $\mathbf{r}$ . The set  $\mathbb{K}(\mathbf{r}, L)$  is called a measurement cell. A geometric observable  $f$ , when measured inside a measurement cell  $\mathbb{K}(\mathbf{r}, L)$ , is denoted as  $f(\mathbf{r}, L)$  and called a local observable. An example are local Hadwiger functional densities  $f = \sum_{i=1}^d c_i \psi_i$  with coefficients  $c_i$  as in Hadwigers theorem (18). Here the local quermassintegrals are defined using (12) as

$$\psi_i(\mathbb{P} \cap \mathbb{K}(\mathbf{r}, L)) = \frac{W_i(\mathbb{P} \cap \mathbb{K}(\mathbf{r}, L))}{V_d(\mathbb{K}(\mathbf{r}, L))} \quad (32)$$

for  $i = 1, \dots, d$ . In the following mainly the special case  $d = 3$  will be of interest. For  $d = 3$  the local porosity is defined by setting  $i = 0$ ,

$$\phi(\mathbf{r}, L) = \psi_0(\mathbb{P} \cap \mathbb{K}(\mathbf{r}, L)). \quad (33)$$

Local densities of surface area, mean curvature and Euler characteristic may be defined analogously. The local porosity distribution, defined as

$$\mu(\phi; \mathbf{r}, L) = \langle \delta(\phi - \phi(\mathbf{r}, L)) \rangle, \tag{34}$$

gives the probability density to find a local porosity  $\phi(\mathbf{r}, L)$  in the measurement cell  $\mathbb{K}(\mathbf{r}, L)$ . Here  $\delta(x)$  denotes the Dirac  $\delta$ -distribution. The support of  $\mu$  is the unit interval. For noncubic measurement cells  $\mathbb{K}$  one defines analogously  $\mu(\phi; \mathbb{K}) = \langle \delta(\phi - \phi(\mathbb{K})) \rangle$  where  $\phi(\mathbb{K}) = \phi(\mathbb{P} \cap \mathbb{K})$  is the local observable in cell  $\mathbb{K}$ .

The concept of local porosity distributions (or more generally “local geometry distributions” [28,30]) was introduced in [27] and has been generalized in two directions [30]. Firstly by admitting more than one measurement cell, and secondly by admitting more than one geometric observable. The general  $n$ -cell distribution function is defined as [30]

$$\begin{aligned} \mu_{n;f_1,\dots,f_m}(f_{11},\dots,f_{1n};\dots;f_{n1},\dots,f_{nm};\mathbb{K}_1,\dots,\mathbb{K}_n) = \\ \langle \delta(f_{11} - f_1(\mathbb{K}_1)) \dots \delta(f_{1n} - f_1(\mathbb{K}_n)) \dots \delta(f_{m1} - f_m(\mathbb{K}_1)) \dots \delta(f_{mn} - f_m(\mathbb{K}_n)) \rangle \end{aligned} \tag{35}$$

for  $n$  general measurement cells  $\mathbb{K}_1, \dots, \mathbb{K}_n$  and  $m$  observables  $f_1, \dots, f_m$ . The  $n$ -cell distribution is the probability density to find the values  $f_{11}$  of the local observable  $f_1$  in cell  $\mathbb{K}_1$  and  $f_{12}$  in cell  $\mathbb{K}_2$  and so on until  $f_{mn}$  of local observable  $f_m$  in  $\mathbb{K}_n$ . Definition (35) is a broad generalization of (34). This generalization is not purely academic, but was motivated by problems of fluid flow in porous media where not only  $\psi_0$  but also  $\psi_1$  becomes important [28]. Local quermassintegrals, defined in (32), and their linear combinations (Hadwiger functionals) furnish important examples for local observables in (35), and they have recently been measured [40].

The general  $n$ -cell distribution is very general indeed. It even contains  $p$  from (24) as the special case  $m = 1, f_1 = \phi$  and  $n = N$  with  $\mathbb{K}_i = \mathbb{V}_i = \mathbb{K}(\mathbf{r}_i, a)$ . More precisely one has

$$\mu_{N;\phi}(\phi_1, \dots, \phi_N; \mathbb{V}_1, \dots, \mathbb{V}_N) = p(\phi_1, \dots, \phi_N) \tag{36}$$

because in that case  $\phi_i = z_i = 1$  if  $\mathbb{V}_i \in \mathbb{P}$  and  $\phi_i = z_i = 0$  for  $\mathbb{V} \notin \mathbb{P}$ . In this way it is seen that the very definition of a stochastic geometry is related to local porosity distributions (or more generally local geometry distributions). As a consequence the general  $n$ -cell distribution  $\mu_{n;f_1,\dots,f_m}$  is again mainly of theoretical interest, and usually unavailable for practical computations.

Expectation values with respect to  $p$  have generalizations to averages with respect to  $\mu$ . Averaging with respect to  $\mu$  will be denoted by an overline. In the

special case  $m = 1, f_1 = \phi$  and  $\mathbb{K}_i = \mathbb{V}_i = \mathbb{K}(\mathbf{r}_i, a)$  with  $n < N$  one finds [30]

$$\begin{aligned}
 & \overline{\phi(\mathbf{r}_1, a) \cdots \phi(\mathbf{r}_n, a)} \\
 &= \int_0^1 \cdots \int_0^1 \phi_1 \cdots \phi_n \mu_{n;\phi}(\phi_1, \dots, \phi_n; \mathbb{V}_1, \dots, \mathbb{V}_n) d\phi_1 \cdots d\phi_n \\
 &= \int_0^1 \cdots \int_0^1 \phi_1 \cdots \phi_n \mu_{N;\phi}(\phi_1, \dots, \phi_N; \mathbb{V}_1, \dots, \mathbb{V}_N) d\phi_1 \cdots d\phi_N \\
 &= \int_0^1 \cdots \int_0^1 \phi_1 \cdots \phi_n \langle \delta(\phi_1 - \phi(\mathbf{r}_1, a)) \cdots \delta(\phi_n - \phi(\mathbf{r}_n, a)) \rangle d\phi_1 \cdots d\phi_n \\
 &= \langle \phi(\mathbf{r}_1, a) \cdots \phi(\mathbf{r}_n, a) \rangle \\
 &= \langle \chi_{\mathbb{P}}(\mathbf{r}_1) \cdots \chi_{\mathbb{P}}(\mathbf{r}_n) \rangle \\
 &= S_n(\mathbf{r}_1, \dots, \mathbf{r}_n)
 \end{aligned} \tag{37}$$

thereby identifying the moment functions of order  $n$  as averages with respect to an  $n$ -cell distribution.

For practical applications the 1-cell local porosity distributions  $\mu(\mathbf{r}, L)$  and their analogues for other quermassintegrals are of greatest interest. For a homogeneous medium the local porosity distribution obeys

$$\mu(\phi; \mathbf{r}, L) = \mu(\phi; \mathbf{0}, L) = \mu(\phi; L) \tag{38}$$

for all lattice vectors  $\mathbf{r}$ , i.e. it is independent of the placement of the measurement cell. A disordered medium with substitutional disorder [71] may be viewed as a stochastic geometry obtained by placing random elements at the cells or sites of a fixed regular substitution lattice. For a substitutionally disordered medium the local porosity distribution  $\mu(\mathbf{r}, L)$  is a periodic function of  $\mathbf{r}$  whose period is the lattice constant of the substitution lattice. For stereological issues in the measurement of  $\mu$  from thin sections see [64].

Averages with respect to  $\mu$  are denoted by an overline. For a homogeneous medium the average local porosity is found as

$$\overline{\phi}(\mathbf{r}, L) = \int_0^1 \mu(\phi; \mathbf{r}, L) d\phi = \langle \phi \rangle = \overline{\phi} \tag{39}$$

independent of  $\mathbf{r}$  and  $L$ . The variance of local porosities for a homogeneous medium defined in the first equality

$$\begin{aligned} \sigma^2(L) &= \overline{(\phi(L) - \bar{\phi})^2} = \int_0^1 (\phi(L) - \bar{\phi})^2 \mu(\phi; L) d\phi \\ &= \frac{1}{L^3} \langle \phi \rangle (1 - \langle \phi \rangle) \left( 1 + \frac{2}{L^3} \sum_{\substack{\mathbf{r}_i, \mathbf{r}_j \in \mathbb{K}(\mathbf{r}_0, L) \\ i \neq j}} G(\mathbf{r}_i - \mathbf{r}_j) \right) \end{aligned} \tag{40}$$

is related to the correlation function as given in the second equality [30]. The skewness of the local porosity distribution is defined as the average

$$\kappa_3(L) = \frac{\overline{(\phi(L) - \bar{\phi})^3}}{\sigma(L)^3} \tag{41}$$

The limits  $L \rightarrow 0$  and  $L \rightarrow \infty$  of small resp. large measurement cells are of special interest. In the first case one reaches the limiting resolution at  $L = a$  and finds for a homogeneous medium [27,30]

$$\mu(\phi; a) = \bar{\phi} \delta(\phi - 1) - (1 - \bar{\phi}) \delta(\phi). \tag{42}$$

The limit  $L \rightarrow \infty$  is more intricate because it requires also the limit  $\mathbb{S} \rightarrow \mathbb{R}^3$ . For a homogeneous medium (40) shows  $\sigma(L) \rightarrow 0$  for  $L \rightarrow 0$  and this suggests

$$\mu(\phi, L \rightarrow \infty) = \delta(\phi - \bar{\phi}). \tag{43}$$

For macroscopically heterogeneous media, however, the limiting distribution may deviate from this result [30]. If (43) holds then in both limits the geometrical information contained in  $\mu$  reduces to the single number  $\bar{\phi} = \langle \phi \rangle$ . If (42) and (43) hold there exists a special length scale  $L^*$  defined as

$$L^* = \min\{L : \mu(0; L) = \mu(1; L) = 0\} \tag{44}$$

at which the  $\delta$ -components at  $\phi = 0$  and  $\phi = 1$  vanish. In the examples below the length  $L^*$  is a measure for the size of pores.

The ensemble picture underlying the definition of a stochastic medium is an idealization. In practice one is given only a single realization and has to resort to an ergodic hypothesis for obtaining an estimate of the local porosity distributions. In the examples below the local porosity distribution is estimated by

$$\tilde{\mu}(\phi; L) = \frac{1}{m} \sum_{\mathbf{r}} \delta(\phi - \phi(\mathbf{r}, L)) \tag{45}$$

where  $m$  is the number of placements of the measurement cell  $\mathbb{K}(\mathbf{r}, L)$ . Ideally the measurement cells should be far apart or at least nonoverlapping, but in

practice this restriction cannot be observed because the samples are not large enough. In the results presented below  $\mathbb{K}(\mathbf{r}, L)$  is placed on all lattice sites which are at least a distance  $L/2$  from the boundary of  $\mathbb{S}$ . This allows for

$$m = \prod_{i=1}^3 (M_i - L + 1) \tag{46}$$

placements of  $\mathbb{K}(\mathbf{r}, L)$  in a sample with side lengths  $M_1, M_2, M_3$ . The use of  $\tilde{\mu}$  instead of  $\mu$  can lead to deviations due to violations of the ergodic hypothesis or simply due to oversampling the central regions of  $\mathbb{S}$  [10,11].

### 3.7 Local Percolation Probabilities

Transport and propagation in porous media are controlled by the connectivity of the pore space. Local percolation probabilities characterize the connectivity [27]. Their calculation requires a three-dimensional pore space representation, and early results were restricted to samples reconstructed laboriously from sequential thin sectioning [32]

Consider the functional  $\Lambda : \mathcal{K} \times \mathcal{K} \times \mathcal{R} \rightarrow \mathbb{Z}_2 = \{0, 1\}$  defined by

$$\Lambda(\mathbb{K}_0, \mathbb{K}_\infty; \mathbb{P} \cap \mathbb{S}) = \begin{cases} 1 & \text{if } \mathbb{K}_0 \rightsquigarrow \mathbb{K}_\infty \text{ in } \mathbb{P} \\ 0 & \text{otherwise} \end{cases} \tag{47}$$

where  $\mathbb{K}_0 \subset \mathbb{R}^3, \mathbb{K}_\infty \subset \mathbb{R}^3$  are two compact convex sets with  $\mathbb{K}_0 \cap (\mathbb{P} \cap \mathbb{S}) \neq \emptyset$  and  $\mathbb{K}_\infty \cap (\mathbb{P} \cap \mathbb{S}) \neq \emptyset$ , and “ $\mathbb{K}_0 \rightsquigarrow \mathbb{K}_\infty$  in  $\mathbb{P}$ ” means that there is a path connecting  $\mathbb{K}_0$  and  $\mathbb{K}_\infty$  that lies completely in  $\mathbb{P}$ . In the examples below the sets  $\mathbb{K}_0$  and  $\mathbb{K}_\infty$  correspond to opposite faces of the sample, but in general other choices are allowed. Analogous to  $\Lambda$  defined for the whole sample one defines for a measurement cell

$$A_\alpha(\mathbf{r}, L) = \Lambda(\mathbb{K}_{0\alpha}, \mathbb{K}_{\infty\alpha}; \mathbb{P} \cap \mathbb{K}(\mathbf{r}, L)) = \begin{cases} 1 & \text{if } \mathbb{K}_{0\alpha} \rightsquigarrow \mathbb{K}_{\infty\alpha} \text{ in } \mathbb{P} \\ 0 & \text{otherwise} \end{cases} \tag{48}$$

where  $\alpha = x, y, z$  and  $\mathbb{K}_{0x}, \mathbb{K}_{\infty x}$  denote those two faces of  $\mathbb{K}(\mathbf{r}, L)$  that are normal to the  $x$  direction. Similarly  $\mathbb{K}_{0y}, \mathbb{K}_{\infty y}, \mathbb{K}_{0z}, \mathbb{K}_{\infty z}$  denote the faces of  $\mathbb{K}(\mathbf{r}, L)$  normal to the  $y$ - and  $z$ -directions. Two additional percolation observables  $A_3$  and  $A_c$  are introduced by

$$A_3(\mathbf{r}, L) = A_x(\mathbf{r}, L)A_y(\mathbf{r}, L)A_z(\mathbf{r}, L) \tag{49}$$

$$A_c(\mathbf{r}, L) = \text{sgn}(A_x(\mathbf{r}, L) + A_y(\mathbf{r}, L) + A_z(\mathbf{r}, L)). \tag{50}$$

$A_3$  indicates that the cell is percolating in all three directions while  $A_c$  indicates percolation in  $x$ - or  $y$ -  $z$ -direction. The local percolation probabilities are defined as

$$\lambda_\alpha(\phi; L) = \frac{\sum_{\mathbf{r}} A_\alpha(\mathbf{r}, L)\delta_{\phi, \phi(\mathbf{r}, L)}}{\sum_{\mathbf{r}} \delta_{\phi, \phi(\mathbf{r}, L)}} \tag{51}$$

where

$$\delta_{\phi, \phi(\mathbf{r}, L)} = \begin{cases} 1 & \text{if } \phi = \phi(\mathbf{r}, L) \\ 0 & \text{otherwise.} \end{cases} \tag{52}$$

The local percolation probability  $\lambda_\alpha(\phi; L)$  gives the fraction of measurement cells of sidelength  $L$  with local porosity  $\phi$  that are percolating in the “ $\alpha$ ”-direction. The total fraction of cells percolating along the “ $\alpha$ ”-direction is then obtained by integration

$$p_\alpha(L) = \int_0^1 \mu(\phi; L) \lambda_\alpha(\phi; L) d\phi. \tag{53}$$

This geometric observable is a quantitative measure for the number of elements that have to be percolating if the pore space geometry is approximated by a substitutionally disordered lattice or network model. Note that neither  $\Lambda$  nor  $\Lambda_\alpha$  are additive functionals, and hence local percolation probabilities have nothing to do with Hadwiger’s theorem.

It is interesting that there is a relation between the local percolation probabilities and the local Euler characteristic  $V_0(\mathbb{P} \cap \mathbb{K}(\mathbf{r}, l))$ . The relation arises from the observation that the voxels  $\mathbb{V}_i$  are closed, convex sets, and hence for any two voxels  $\mathbb{V}_i, \mathbb{V}_j$  the Euler characteristic of their intersection

$$V_0(\mathbb{V}_i \cap \mathbb{V}_j) = \begin{cases} 1 & \text{if } \mathbb{V}_i \cap \mathbb{V}_j \neq \emptyset \\ 0 & \text{if } \mathbb{V}_i \cap \mathbb{V}_j = \emptyset \end{cases} \tag{54}$$

indicates whether two voxels are nearest neighbours. A measurement cell  $\mathbb{K}(\mathbf{r}, L)$  contains  $L^3$  voxels. It is then possible to construct a  $(L^3 + 2) \times (L^3 + 2)^2$ -matrix  $B$  with matrix elements

$$(B)_{i (i,j)} = V_0(\mathbb{V}_i \cap \mathbb{V}_j) \tag{55}$$

$$(B)_{i (j,i)} = -V_0(\mathbb{V}_i \cap \mathbb{V}_j) \tag{56}$$

where  $i, j \in \{0, 1, \dots, L^3, \infty\}$  and the sets  $\mathbb{V}_0 = \mathbb{K}_0$  and  $\mathbb{V}_\infty = \mathbb{K}_\infty$  are two opposite faces of the measurement cell. The rows in the matrix  $B$  correspond to voxels while the columns correspond to voxel pairs. Define the matrix  $A = BB^T$  where  $B^T$  is the transpose of  $B$ . The diagonal elements  $(A)_{ii}$  give the number of voxels to which the voxel  $\mathbb{V}_i$  is connected. A matrix element  $(A)_{ij}$  differs from zero if and only if  $\mathbb{V}_i$  and  $\mathbb{V}_j$  are connected. Hence the matrix  $A$  reflects the local connectedness of the pore space around a single voxel. Sufficiently high powers of  $A$  provide information about the global connectedness of  $\mathbb{P}$ . One finds

$$\Lambda(\mathbb{K}_0, \mathbb{K}_\infty; \mathbb{P} \cap \mathbb{K}(\mathbf{r}, L)) = \text{sgn} (|(A^m)_{0\infty}|) \tag{57}$$

where  $(A^m)_{0\infty}$  is the matrix element in the upper right hand corner and  $m$  is arbitrary subject to the condition  $m > L^3$ . The set  $\mathbb{P} \cap \mathbb{K}(\mathbf{r}, L)$  can always be

decomposed uniquely into pairwise disjoint connectedness components (clusters)  $\mathbb{B}_i$  whose number is given by the rank of  $B$ . Hence

$$V_0(\mathbb{P} \cap \mathbb{K}(\mathbf{r}, L)) = \sum_{i=1}^{\text{rank} B} V_0(\mathbb{B}_i) \tag{58}$$

provides an indirect connection between the local Euler characteristic and the local percolation probabilities mediated by the matrix  $B$ . (For percolation systems it has been conjectured that the zero of the Euler characteristic as a function of the occupation probability is an approximation to the percolation threshold [45].)

## 4 Stochastic Reconstruction of Microstructures

### 4.1 Description of Experimental Sample

The experimental sample, denoted as  $\mathbb{S}_{\text{EX}}$ , is a three-dimensional microtomographic image of Fontainebleau sandstone. This sandstone is a popular reference standard because of its chemical, crystallographic and microstructural simplicity [13,14]. Fontainebleau sandstone consists of monocrystalline quartz grains that have been eroded for long periods before being deposited in dunes along the sea shore during the Oligocene, roughly 30 million years ago. It is well sorted containing grains of around  $200\mu\text{m}$  in diameter. The sand was cemented by silica crystallizing around the grains. Fontainebleau sandstone exhibits intergranular porosity ranging from 0.03 to roughly 0.3 [13].

**Table 2.** Overview of geometric properties of the four microstructures displayed in Figs. 1 through 4

Properties	$\mathbb{S}_{\text{EX}}$	$\mathbb{S}_{\text{DM}}$	$\mathbb{S}_{\text{GF}}$	$\mathbb{S}_{\text{SA}}$
$M_1$	300	255	256	256
$M_2$	300	255	256	256
$M_3$	299	255	256	256
$\phi(\mathbb{P} \cap \mathbb{S})$	0.1355	0.1356	0.1421	0.1354
$\phi_2(\mathbb{P} \cap \mathbb{S})$	$10.4\text{mm}^{-1}$	$10.9\text{mm}^{-1}$	$16.7\text{mm}^{-1}$	$11.06\text{mm}^{-1}$
$L^*$	35	25	23	27
$1 - \lambda_c(0.1355, L^*)$	0.0045	0.0239	0.3368	0.3527

The computer assisted microtomography was carried out on a micro-plug drilled from a larger original core. The original core from which the micro-plug was taken had a measured porosity of 0.1484, permability of  $1.3D$  and formation factor 22.1. The porosity  $\phi(\mathbb{S}_{\text{EX}})$  of the microtomographic data set is only 0.1355(see Table 2). The difference between the porosity of the original core and that of the final data set is due to the heterogeneity of the sandstone and to the difference in sample size. The experimental sample is referred to as EX in the following. The pore space of the experimental sample is visualized in Fig. 1.

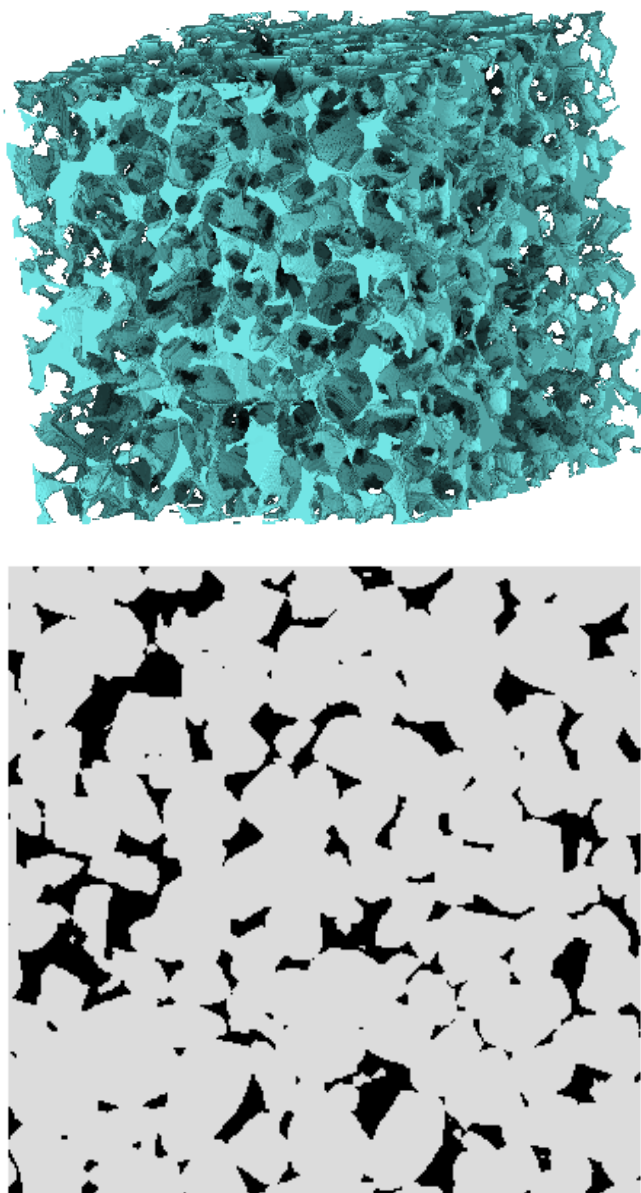


**Fig. 1.** Sample EX: Threedimensional pore space  $\mathbb{P}_{\text{EX}}$  of Fontainebleau sandstone. The resolution of the image is  $a = 7.5\mu\text{m}$ , the sample dimensions are  $M_1 = 300$ ,  $M_2 = 300$ ,  $M_3 = 299$ . The pore space is indicated opaque, the matrix space is transparent. The lower image shows the front plane of the sample as a twodimensional thin section (pore space black, matrix grey).

## 4.2 Sedimentation, Compaction and Diagenesis Model

Fontainebleau sandstone is the result of complex physical, chemical and geological processes known as sedimentation, compaction and diagenesis. It is therefore natural to model these processes directly rather than trying to match general geometrical characteristics. This conclusion was also obtained from local porosity theory for the cementation index in Archie's law [27]. The diagenesis model abbreviated as DM in the following, attempts model the main geological sandstone-forming processes [4,48].

In a first step porosity, grain size distribution, a visual estimate of the degree of compaction, the amount of quartz cement and clay contents and texture are obtained by image analysis of backscattered electron/cathodo-luminescence images made from thin sections. The sandstone modeling is then carried out in three main steps: grain sedimentation, compaction and diagenesis described in detail in [4,48].

Sedimentation begins by measuring the grain size distribution using an erosion-dilation algorithm. Then spheres with random diameters are picked randomly according to the grain size distribution. They are dropped onto the grain bed and relaxed into a local potential energy minimum or, alternatively, into the global minimum.

Compaction occurs because the sand becomes buried into the subsurface. Compaction reduces the bulk volume (and porosity). It is modelled as a linear process in which the vertical coordinate of every sandgrain is shifted vertically downwards by an amount proportional to the original vertical position. The proportionality constant is called the compaction factor. Its value for the Fontainebleau sample is estimated to be 0.1 from thin section analysis.

In the diagenesis part only a subset of known diagenetical processes are simulated, namely quartz cement overgrowth and precipitation of authigenic clay on the free surface. Quartz cement overgrowth is modeled by radially enlarging each grain. If  $R_0$  denotes the radius of the originally deposited spherical grain, its new radius along the direction  $\mathbf{r}$  from grain center is taken to be [48,59]

$$R(\mathbf{r}) = R_0 + \min(b\ell(\mathbf{r})^\gamma, \ell(\mathbf{r})) \quad (59)$$

where  $\ell(\mathbf{r})$  is the distance between the surface of the original spherical grain and the surface of its Voronoi polyhedron along the direction  $\mathbf{r}$ . The constant  $b$  controls the amount of cement, and the growth exponent  $\gamma$  controls the type of cement overgrowth. For  $\gamma > 0$  the cement grows preferentially into the pore bodies, for  $\gamma = 0$  it grows concentrically, and for  $\gamma < 0$  quartz cement grows towards the pore throats [48]. Authigenic clay growth is simulated by precipitating clay voxels on the free mineral surface. The clay texture may be pore-lining or pore-filling or a combination of the two.

The parameters for modeling the Fontainebleau sandstone were 0.1 for the compaction factor, and  $\gamma = -0.6$  and  $b = 2.9157$  for the cementation parameters. The resulting model configuration of the sample DM is displayed in Fig. 2.

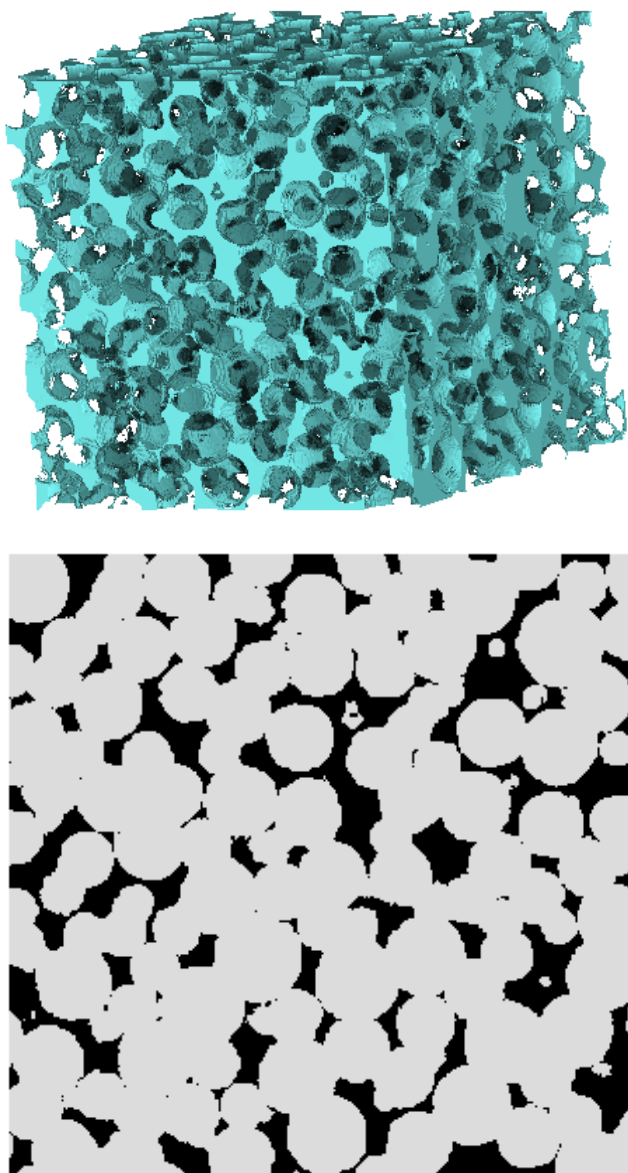


**Fig. 2.** Sample DM: Threedimensional pore space  $\mathbb{P}_{\text{DM}}$  of the sedimentation and diagenesis model described in the text. The resolution is  $a = 7.5\mu\text{m}$ , the sample dimensions are  $M_1 = 255$ ,  $M_2 = 255$ ,  $M_3 = 255$ . The pore space is indicated opaque, the matrix space is transparent. The lower image shows the front plane of the sample as a twodimensional thin section (pore space black, matrix grey)

### 4.3 Gaussian Field Reconstruction Model

A stochastic reconstruction model attempts to approximate a given experimental sample by a randomly generated model structure that matches prescribed stochastic properties of the experimental sample. In this and the next section the stochastic property of interest is the correlation function  $G_{\text{EX}}(\mathbf{r})$  of the Fontainebleau sandstone.

The Gaussian field (GF) reconstruction model tries to match a reference correlation function by filtering Gaussian random variables [1,2,49,69]. Given the reference correlation function  $G_{\text{EX}}(\mathbf{r})$  and porosity  $\phi(\mathbb{S}_{\text{EX}})$  of the experimental sample the Gaussian field method proceeds in three main steps:

1. Initially a Gaussian field  $X(\mathbf{r})$  is generated consisting of statistically independent Gaussian random variables  $X \in \mathbb{R}$  at each lattice point  $\mathbf{r}$ .
2. The field  $X(\mathbf{r})$  is first passed through a linear filter which produces a correlated Gaussian field  $Y(\mathbf{r})$  with zero mean and unit variance. The reference correlation function  $G_{\text{EX}}(\mathbf{r})$  and porosity  $\phi(\mathbb{S}_{\text{EX}})$  enter into the mathematical construction of this linear filter.
3. The correlated field  $Y(\mathbf{r})$  is then passed through a nonlinear discretization filter which produces the reconstructed sample  $\mathbb{S}_{\text{GF}}$ .

Step 2 is costly because it requires the solution of a very large set of non-linear equations. A computationally more efficient method uses Fourier Transformation [1]. The linear filter in step 2 is defined in Fourier space through

$$Y(\mathbf{k}) = \alpha(G_Y(\mathbf{k}))^{\frac{1}{2}}X(\mathbf{k}), \quad (60)$$

where  $M = M_1 = M_2 = M_3$  is the sidelength of a cubic sample,  $\alpha = M^{\frac{d}{2}}$  is a normalisation factor, and

$$X(\mathbf{k}) = \frac{1}{M^d} \sum_{\mathbf{r}} X(\mathbf{r})e^{2\pi i\mathbf{k}\cdot\mathbf{r}} \quad (61)$$

denotes the Fourier transform of  $X(\mathbf{r})$ . Similarly  $Y(\mathbf{k})$  is the Fourier transform of  $Y(\mathbf{r})$ , and  $G_Y(\mathbf{k})$  is the Fourier transform of the correlation function  $G_Y(\mathbf{r})$ .  $G_Y(\mathbf{r})$  has to be computed by an inverse process from the correlation function  $G_{\text{EX}}(\mathbf{r})$  and porosity of the experimental reference (details in [1]).

The Gaussian field reconstruction requires a large separation  $\xi_{\text{EX}} \ll N^{1/d}$  where  $\xi_{\text{EX}}$  is the correlation length of the experimental reference, and  $N = M_1M_2M_3$  is the number of sites.  $\xi_{\text{EX}}$  is defined as the length such that  $G_{\text{EX}}(r) \approx 0$  for  $r > \xi_{\text{EX}}$ . If the condition  $\xi_{\text{EX}} \ll N^{1/d}$  is violated then step 2 of the reconstruction fails in the sense that the correlated Gaussian field  $Y(\mathbf{r})$  does not have zero mean and unit variance. In such a situation the filter  $G_Y(\mathbf{k})$  will differ from the Fourier transform of the correlation function of the  $Y(\mathbf{r})$ . It is also difficult to calculate  $G_Y(r)$  accurately near  $r = 0$  [1]. This leads to a discrepancy at small  $r$  between  $G_{\text{GF}}(r)$  and  $G_{\text{EX}}(r)$ . The problem can be overcome by choosing large  $M$ . However, in  $d = 3$  very large  $M$  also demands prohibitively large memory. In

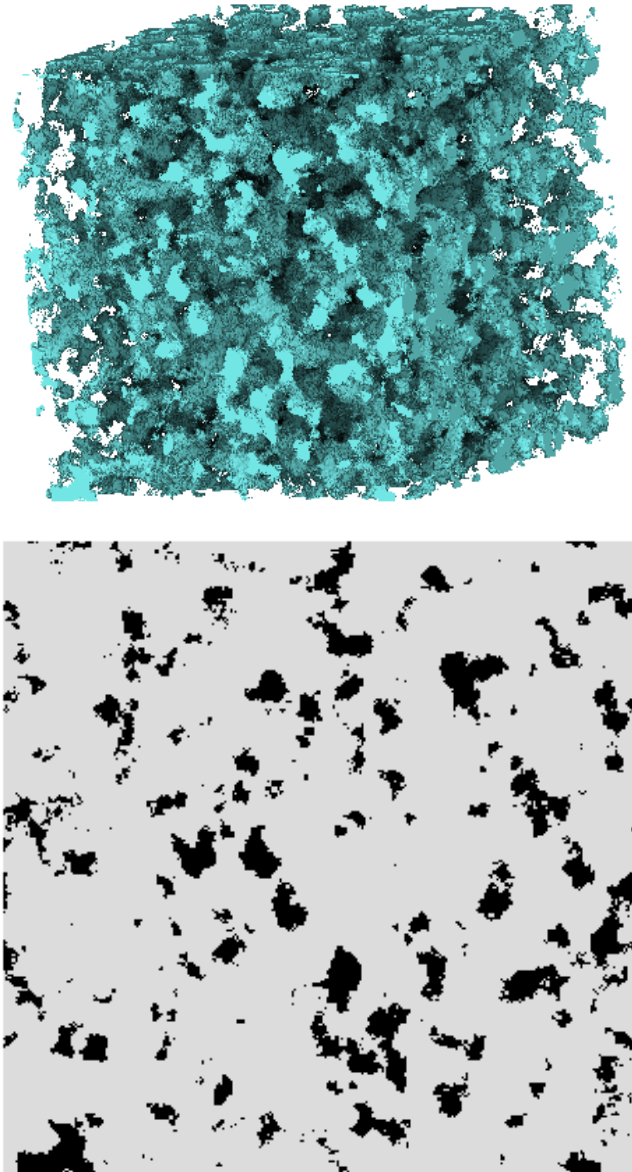


**Fig. 3.** Sample GF: Threedimensional pore space  $\mathbb{P}_{\text{GF}}$  with  $G_{\text{GF}}(r) \approx G_{\text{EX}}(r)$  constructed by filtering Gaussian random fields. The resolution is  $a = 7.5\mu\text{m}$ , the sample dimensions are  $M_1 = 256$ ,  $M_2 = 256$ ,  $M_3 = 256$ . The pore space is indicated opaque, the matrix space is transparent. The lower image shows the front plane of the sample as a twodimensional thin section (pore space black, matrix grey)

earlier work [1,2] the correlation function  $G_{\text{EX}}(\mathbf{r})$  was sampled down to a lower resolution, and the reconstruction algorithm then proceeded with such a rescaled correlation function. This leads to a reconstructed sample  $\mathbb{S}_{\text{GF}}$  which also has a lower resolution. Such reconstructions have lower average connectivity compared to the original model [9]. For a quantitative comparison with the microstructure of  $\mathbb{S}_{\text{EX}}$  it is necessary to retain the original level of resolution, and to use the original correlation function  $G_{\text{EX}}(\mathbf{r})$  without subsampling. Because  $G_{\text{EX}}(r)$  is nearly 0 for  $r > 30a$   $G_{\text{EX}}(r)$  was truncated at  $r = 30a$  to save computer time. The resulting configuration  $\mathbb{S}_{\text{GF}}$  with  $M = 256$  is displayed in Fig. 3.

#### 4.4 Simulated Annealing Reconstruction Model

The simulated annealing (SA) reconstruction model is a second method to generate a three-dimensional random microstructure with prescribed porosity and correlation function. The method generates a configuration  $\mathbb{S}_{\text{SA}}$  by minimizing the deviations between  $G_{\text{SA}}(\mathbf{r})$  and a predefined reference function  $G_0(\mathbf{r})$ . Note that the generated configuration  $\mathbb{S}_{\text{SA}}$  is not unique and hence other modeling aspects come into play [42]. Below,  $G_0(\mathbf{r}) = G_{\text{EX}}(\mathbf{r})$  is again the correlation function of the Fontainebleau sandstone.

An advantage of the simulated annealing method over the Gaussian field method is that it can also be used to match other quantities besides the correlation function. Examples would be the linear or spherical contact distributions [42]. On the other hand the method is computationally very demanding, and cannot be implemented fully at present. A simplified implementation was discussed in [70], and is used below.

The reconstruction is performed on a cubic lattice with side length  $M = M_1 = M_2 = M_3$  and lattice spacing  $a$ . The lattice is initialized randomly with 0's and 1's such that the volume fraction of 0's equals  $\phi(\mathbb{S}_{\text{EX}})$ . This porosity is preserved throughout the simulation. For the sake of numerical efficiency the autocorrelation function is evaluated in a simplified form using [70]

$$\begin{aligned} \tilde{G}_{\text{SA}}(r) \left( \tilde{G}_{\text{SA}}(0) - \tilde{G}_{\text{SA}}(0)^2 \right) + \tilde{G}_{\text{SA}}(0)^2 &= \\ = \frac{1}{3M^3} \sum_{\mathbf{r}} \chi_{\mathbb{M}}(\mathbf{r}) \left( \chi_{\mathbb{M}}(\mathbf{r} + r\mathbf{e}_1) + \chi_{\mathbb{M}}(\mathbf{r} + r\mathbf{e}_2) + \chi_{\mathbb{M}}(\mathbf{r} + r\mathbf{e}_3) \right) \end{aligned} \quad (62)$$

where  $\mathbf{e}_i$  are the unit vectors in direction of the coordinate axes,  $r = 0, \dots, \frac{M}{2} - 1$ , and where a tilde  $\tilde{\phantom{x}}$  is used to indicate the directional restriction. The sum  $\sum_{\mathbf{r}}$  runs over all  $M^3$  lattice sites  $\mathbf{r}$  with periodic boundary conditions, i.e.  $r_i + r$  is evaluated modulo  $M$ .

A simulated annealing algorithm is used to minimize the "energy" function

$$E = \sum_r \left( \tilde{G}_{\text{SA}}(r) - G_{\text{EX}}(r) \right)^2, \quad (63)$$

defined as the sum of the squared deviations of  $\tilde{G}_{\text{SA}}$  from the experimental correlation function  $G_{\text{EX}}$ . Each update starts with the exchange of two pixels, one

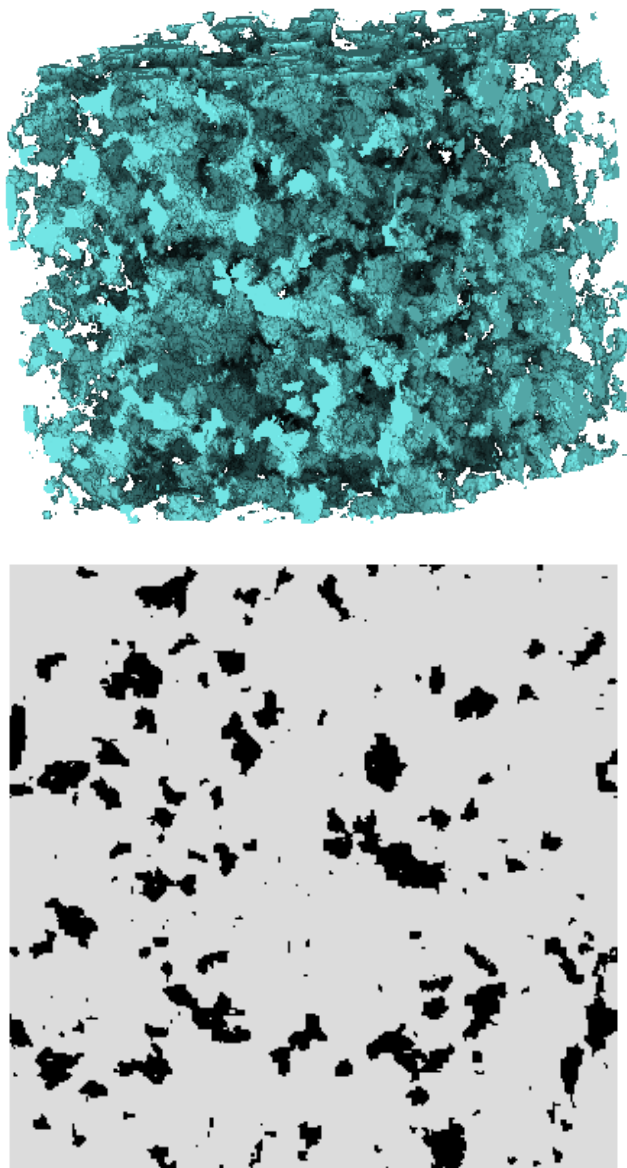


**Fig. 4.** Sample SA: Threedimensional pore space  $\mathbb{P}_{\text{SA}}$  with  $G_{\text{SA}}(r) = G_{\text{EX}}(r)$  constructed using a simulated annealing algorithm. The resolution is  $a = 7.5\mu\text{m}$ , the sample dimensions are  $M_1 = 256$ ,  $M_2 = 256$ ,  $M_3 = 256$ . The pore space is indicated opaque, the matrix space is transparent. The lower image shows the front plane of the sample as a twodimensional thin section (pore space black, matrix grey)

from pore space, one from matrix space. Let  $n$  denote the number of the proposed update step. Introducing an acceptance parameter  $T_n$ , which may be interpreted as an  $n$ -dependent temperature, the proposed configuration is accepted with probability

$$p = \min \left( 1, \exp \left( -\frac{E_n - E_{n-1}}{T_n E_{n-1}} \right) \right). \quad (64)$$

Here the energy and the correlation function of the configuration is denoted as  $E_n$  and  $\tilde{G}_{\text{SA},n}$ , respectively. If the proposed move is rejected, then the old configuration is restored.

A configuration with correlation  $G_{\text{EX}}$  is found by lowering  $T$ . At low  $T$  the system approaches a configuration that minimizes the energy function. In the simulations  $T_n$  was lowered with  $n$  as

$$T_n = \exp \left( -\frac{n}{100000} \right). \quad (65)$$

The simulation was stopped when 20000 consecutive updates were rejected. This happened after  $2.5 \times 10^8$  updates ( $\approx 15$  steps per site). The resulting configuration  $\mathbb{S}_{\text{SA}}$  for the simulated annealing reconstruction is displayed in Fig. 4.

A complete evaluation of the correlation function as defined in (29) for a three-dimensional system requires so much computer time, that it cannot be carried out at present. Therefore the algorithm was simplified to increase its speed [70]. In the simplified algorithm the correlation function is only evaluated along the directions of the coordinate axes as indicated in (62). The original motivation was that for isotropic systems all directions should be equivalent [70]. However, it was found in [41] that as a result of this simplification the reconstructed sample may become anisotropic. In the simplified algorithm the correlation function of the reconstruction deviates from the reference correlation function in all directions other than those of the axes [41]. The problem is illustrated in Figs. 5(a) and 5(b) in two dimensions for a reference correlation function given as

$$G_0(r) = e^{-r/8} \cos r. \quad (66)$$

In Fig. 5a the correlation function was matched only in the direction of the  $x$ - and  $y$ -axis. In Fig. 5b the correlation function was matched also along the diagonal directions obtained by rotating the axes 45 degrees. The differences in isotropy of the two reconstructions are clearly visible. In the special case of the correlation function of the Fontainebleau sandstone, however, this effect seems to be smaller. The Fontainebleau correlation function is given in Fig. 7 below. Figure 6a and 6b show the result of twodimensional reconstructions along the axes only and along axes plus diagonal directions. The differences in isotropy seem to be less pronounced. Perhaps this is due to the fact that the Fontainebleau correlation function has no maxima and minima.

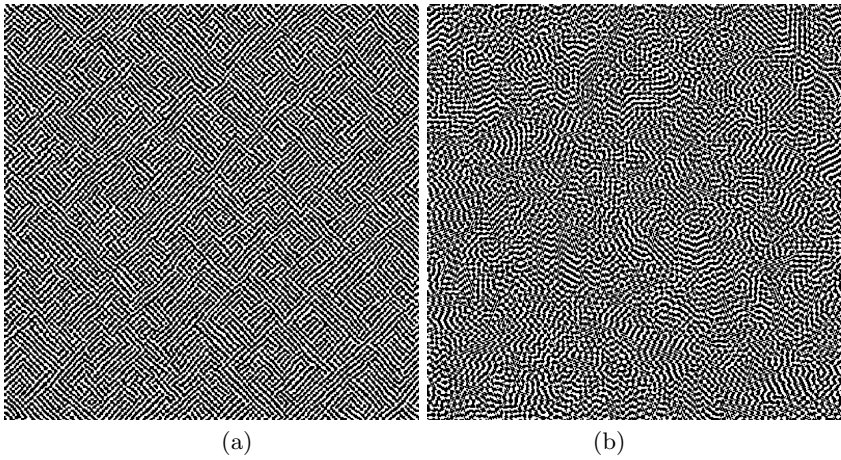


**Fig. 5.** Twodimensional stochastic reconstruction for the correlation function of  $G_0(r) = e^{-r/8} \cos r$  (a) for the direction of the  $x$ - and  $y$ -coordinate axes only, and (b) for the directions of the coordinate axes plus diagonal directions.

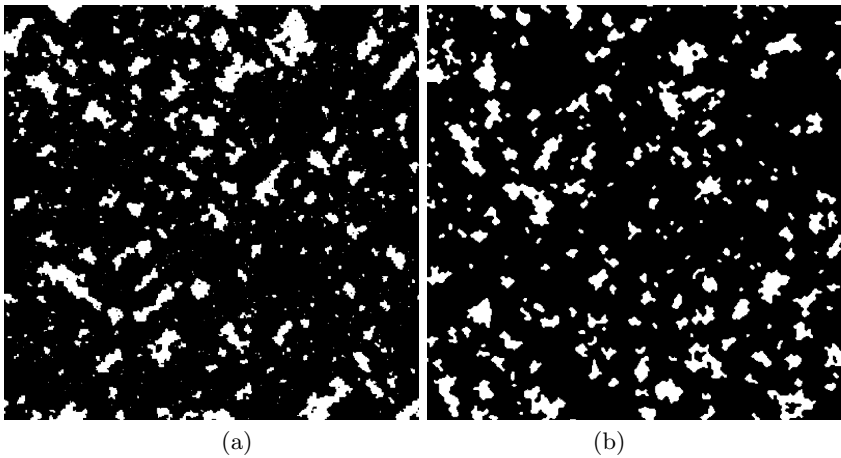


**Fig. 6.** A Twodimensional stochastic reconstruction for the correlation function  $G_0(r) = G_{\text{EX}}(r)$  displayed as the solid line in Fig. 7a along the direction of the  $x$ - and  $y$ -coordinate axes only, and Fig. 7b along the directions of the coordinate axes plus diagonal directions.

## 5 Quantitative Comparison of Microstructures

### 5.1 Conventional Observables and Correlation Functions

Table 2 gives an overview of several geometric properties for the four microstructures discussed in the previous section. Samples GF and SA were constructed to have the same correlation function as sample EX. Figure 7 shows the direction-

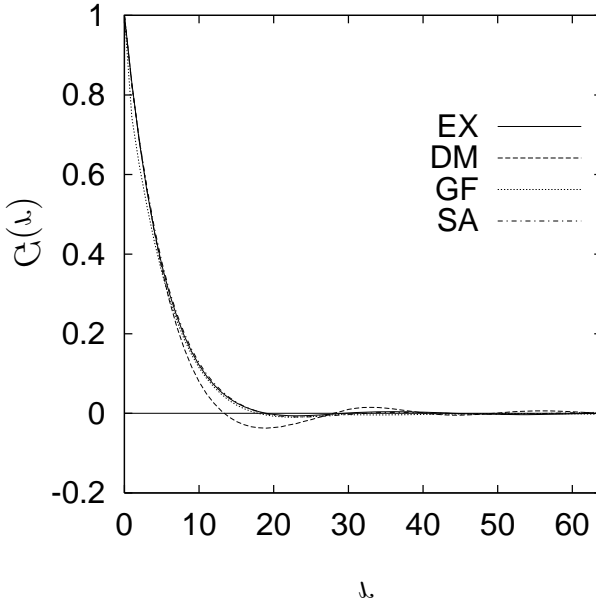


**Fig. 7.** Directionally averaged correlation functions  $G(r) = (G(r, 0, 0) + G(0, r, 0) + G(0, 0, r))/3$  of the samples EX,DM,GF and SA

ally averaged correlation functions  $G(r) = (G(r, 0, 0) + G(0, r, 0) + G(0, 0, r))/3$  of all four microstructures where the notation  $G(r_1, r_2, r_3) = G(\mathbf{r})$  was used.

The Gaussian field reconstruction  $G_{GF}(r)$  is not perfect and differs from  $G_{EX}(r)$  for small  $r$ . The discrepancy at small  $r$  reflects the quality of the linear filter, and it is also responsible for the differences of the porosity and specific internal surface. Also, by construction,  $G_{GF}(r)$  is not expected to equal  $G_{EX}(r)$  for  $r$  larger than 30. Although the reconstruction method of sample  $S_{SA}$  is intrinsically anisotropic the correlation function of sample SA agrees also in the diagonal directions with that of sample EX. Sample  $S_{DM}$  while matching the porosity and grain size distribution was not constructed to match also the correlation function. As a consequence  $G_{DM}(r)$  differs clearly from the rest. It reflects the grain structure of the model by becoming negative.  $G_{DM}(r)$  is also anisotropic.

If two samples have the same correlation function they are expected to have also the same specific internal surface as calculated from

$$S = -4 \langle \phi \rangle (1 - \langle \phi \rangle) \left. \frac{dG(r)}{dr} \right|_{r=0}. \quad (67)$$

The specific internal surface area calculated from this formula is given in Table 2 for all four microstructures.

If one defines a decay length by the first zero of the correlation function then the decay length is roughly  $18a$  for samples EX, GF and SA. For sample DM it is somewhat smaller mainly in the  $x$ - and  $y$ -direction. The correlation length, which will be of the order of the decay length, is thus relatively large compared to the system size. Combined with the fact that the percolation threshold for continuum systems is typically around 0.15 this might explain why models GF and SA are connected in spite of their low value of the porosity.

In summary, the samples  $\mathbb{S}_{\text{GF}}$  and  $\mathbb{S}_{\text{SA}}$  were constructed to be indistinguishable with respect to porosity and correlations from  $\mathbb{S}_{\text{EX}}$ . Sample SA comes close to this goal. The imperfection of the reconstruction method for sample GF accounts for the deviations of its correlation function at small  $r$  from that of sample EX. Although the difference in porosity and specific surface is much bigger between samples SA and GF than between samples SA and EX sample SA is in fact more similar to GF than to EX in a way that can be quantified using local porosity analysis. Traditional characteristics such as porosity, specific surface and correlation functions are insufficient to distinguish different microstructures. Visual inspection of the pore space indicates that samples GF and SA have a similar structure which, however, differs from the structure of sample EX. Although sample DM resembles sample EX more closely with respect to surface roughness it differs visibly in the shape of the grains.

## 5.2 Local Porosity Analysis

The differences in visual appearance of the four microstructures can be quantified using the geometric observables  $\mu$  and  $\lambda$  from local porosity theory. The local porosity distributions  $\mu(\phi, 20)$  of the four samples at  $L = 20a$  are displayed as the solid lines in Figs. 8a through 8d. The ordinates for these curves are plotted on the right vertical axis.

The figures show that the original sample exhibits stronger porosity fluctuations than the three model samples except for sample SA which comes close. Sample DM has the narrowest distribution which indicates that it is most homogeneous. Figures 8a–8d show also that the  $\delta$ -function component at the origin,  $\mu(0, 20)$ , is largest for sample EX, and smallest for sample GF. For samples DM and SA the values of  $\mu(0, 20)$  are intermediate and comparable. Plotting  $\mu(0, L)$  as a function of  $L$  shows that this remains true for all  $L$ . These results indicate that the experimental sample EX is more strongly heterogeneous than the models, and that large regions of matrix space occur more frequently in sample EX. A similar conclusion may be drawn from the variance of local porosity

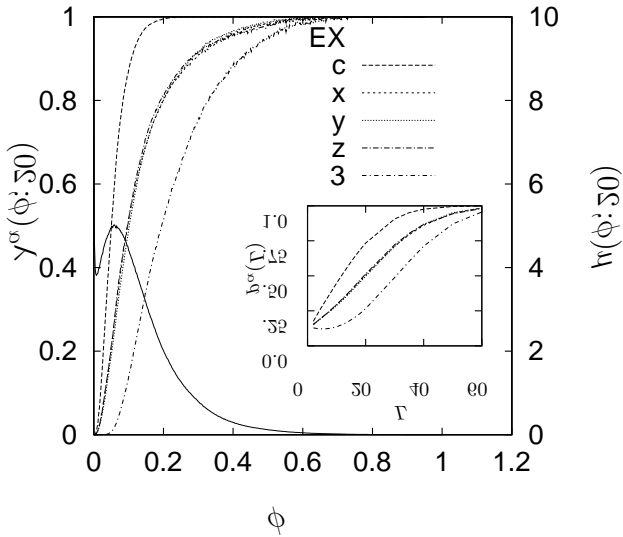


Figure 8a

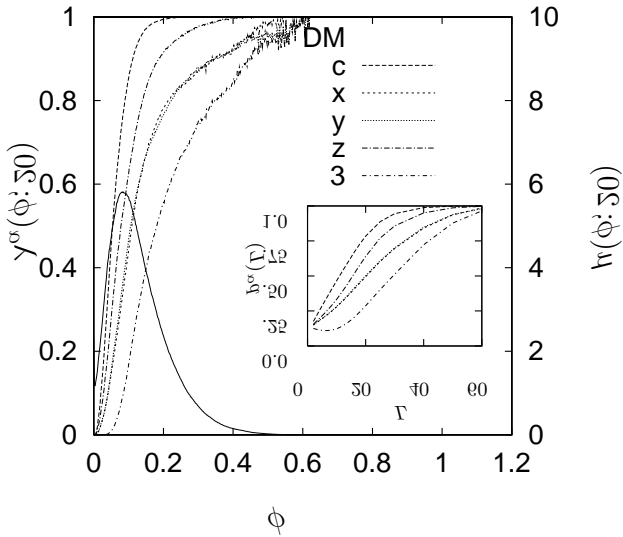


Figure 8b

**Fig. 8.** Local percolation probabilities  $\lambda_\alpha(\phi, 20)$  (broken curves, values on left axis) and local porosity distribution  $\mu(\phi, 20)$  (solid curve, values on right axis) at  $L = 20$  for sample EX(Fig. 8a), sample DM(Fig. 8b), sample GF(Fig. 8c), and sample SA(Fig. 8d). The inset shows the function  $p_\alpha(L)$ . The line styles corresponding to  $\alpha = c, x, y, z, 3$  are indicated in the legend.

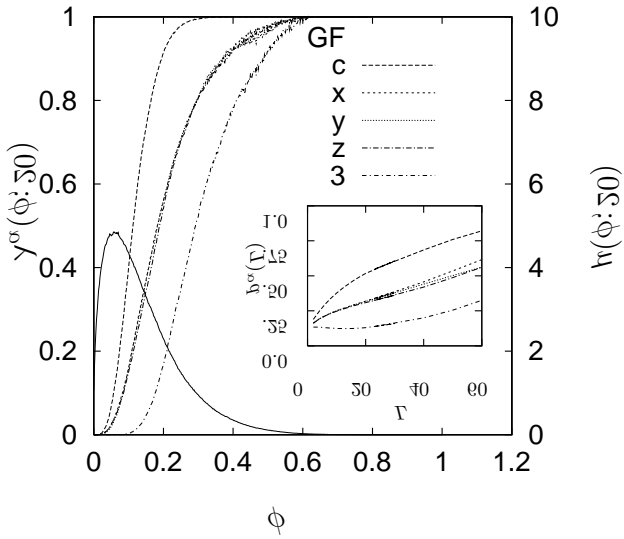


Figure 8c

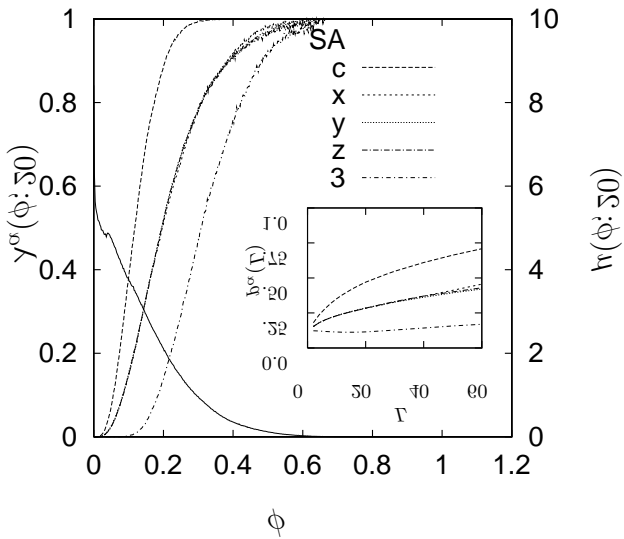
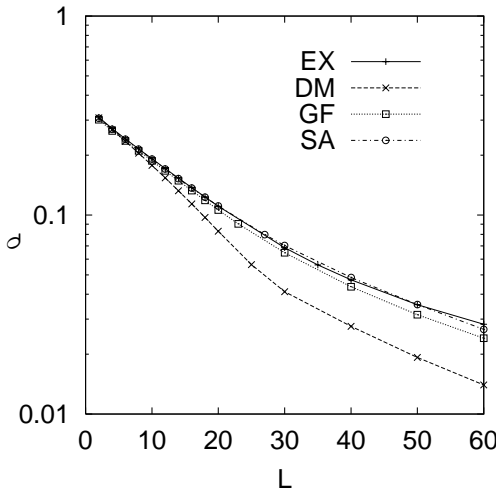


Figure 8d

fluctuations which will be studied below. The conclusion is also consistent with the results for  $L^*$  shown in Table 2.  $L^*$  gives the sidelength of the largest cube that can be fit into matrix space, and thus  $L^*$  may be viewed as a measure for the size of the largest grain. Table 2 shows that the experimental sample has a larger  $L^*$  than all the models. It is interesting to note that plotting  $\mu(1, L)$  versus  $L$  also shows that the curve for the experimental sample lies above those for the other samples for all  $L$ . Thus, also the size of the largest pore and the pore space heterogeneity are largest for sample EX. If  $\mu(\phi, L^*)$  is plotted for all four samples one finds two groups. The first group is formed by samples EX and DM, the second by samples GF and SA. Within each group the curves  $\mu(\phi, L^*)$  nearly overlap, but they differ strongly between them.

Figures 9 and 10 exhibit the dependence of the local porosity fluctuations on  $L$ . Figure 9 shows the variance of the local porosity fluctuations, defined in



**Fig. 9.** Variance of local porosities for sample EX(solid line with tick), DM(dashed line with cross), GF(dotted line with square), and SA(dash-dotted line with circle).

(40) as function of  $L$ . The variances for all samples indicate an approach to a  $\delta$ -distribution according to (43). Again sample DM is most homogeneous in the sense that its variance is smallest. The agreement between samples EX, GF and SA reflects the agreement of their correlation functions, and is expected by virtue of eq. (40). Figure 10 shows the skewness as a function of  $L$  calculated from (41).  $\kappa_3$  characterizes the asymmetry of the distribution, and the difference between the most probable local porosity and its average. Again samples GF and SA behave similarly, but sample DM and sample EX differ from each other, and from the rest.

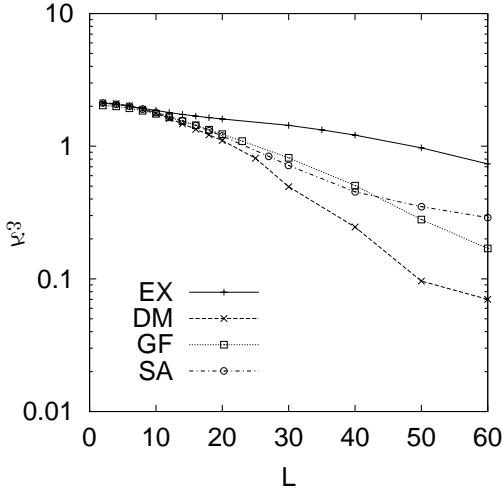


**Fig. 10.** Skewness of local porosities for sample EX(solid line with tick), DM(dashed line with cross), GF(dotted line with square), and SA(dash-dotted line with circle).

At  $L = 4a$  the local porosity distributions  $\mu(\phi, 4)$  show small spikes at equidistantly spaced porosities for samples EX and DM, but not for samples GF and SA. The spikes indicate that models EX and DM have a smoother surface than models GF and SA. For smooth surfaces and small measurement cell size porosities corresponding to an interface intersecting the measurement cell produce a finite probability for certain porosities because the discretized interface allows only certain volume fractions. In general whenever a certain porosity occurs with finite probability this leads to spikes in  $\mu$ .

### 5.3 Local Percolation Analysis

Visual inspection of Figs. 1 through 4 does not reveal the degree of connectivity of the various samples. A quantitative characterization of connectivity is provided by local percolation probabilities [10,27], and it is here that the samples differ most dramatically.

The samples EX, DM, GF and SA are globally connected in all three directions. This, however, does not imply that they have similar connectivity. The last line in Table 2 gives the fraction of blocking cells at the porosity 0.1355 and for  $L^*$ . It gives a first indication that the connectivity of samples DM and GF is, in fact, much poorer than that of the experimental sample EX.

Figures 8a through 8d give a more complete account of the situation by exhibiting  $\lambda_\alpha(\phi, 20)$  for  $\alpha = 3, c, x, y, z$  for all four samples. First one notes that sample DM is strongly anisotropic in its connectivity. It has a higher connectivity

in the  $z$ -direction than in the  $x$ - or  $y$ -direction. This was found to be partly due to the coarse grid used in the sedimentation algorithm [47].  $\lambda_z(\phi, 20)$  for sample DM differs from that of sample EX although their correlation functions in the  $z$ -direction are very similar. The  $\lambda$ -functions for samples EX and DM rise much more rapidly than those for samples GF and SA. The inflection point of the  $\lambda$ -curves for samples EX and DM is much closer to the most probable porosity (peak) than in samples GF and SA. All of this indicates that connectivity in cells with low porosity is higher for samples EX and DM than for samples GF and SA. In samples GF and SA only cells with high porosity are percolating on average. In sample DM the curves  $\lambda_x, \lambda_y$  and  $\lambda_3$  show strong fluctuations for  $\lambda \approx 1$  at values of  $\phi$  much larger than the  $\langle \phi \rangle$  or  $\phi(\mathbb{S}_{DM})$ . This indicates a large number of high porosity cells which are nevertheless blocked. The reason for this is perhaps that the linear compaction process in the underlying model blocks horizontal pore throats and decreases horizontal spatial continuity more effectively than in the vertical direction, as shown in [4], Table 1, p. 142.

The absence of spikes in  $\mu(\phi, 4)$  for samples GF and SA combined with the fact that cells with average porosity ( $\approx 0.135$ ) are rarely percolating suggests that these samples have a random morphology similar to percolation.

The insets in Figs. 8a through 8d show the functions  $p_\alpha(L) = \lambda_\alpha(\phi, L)$  for  $\alpha = 3, x, y, z, c$  for each sample calculated from (53). The curves for samples EX and DM are similar but differ from those for samples GF and SA. Figure 11 exhibits the curves  $p_3(L)$  of all four samples in a single figure. The samples fall

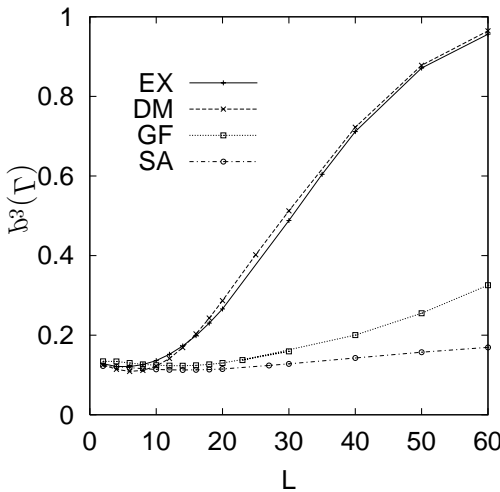


**Fig. 11.**  $p_3(L)$  for sample EX(solid line with tick) DM(dashed line with cross) GF(dotted line with square), and SA(dash-dotted line with circle).

into two groups  $\{EX, DM\}$  and  $\{GF, SA\}$  that behave very differently. Figure 11

suggests that reconstruction methods [1,70] based on correlation functions do not reproduce the connectivity properties of porous media. As a consequence, one expects that also the physical transport properties will differ from the experimental sample, and it appears questionable whether a pure correlation function reconstruction can produce reliable models for the prediction of transport.

Preliminary results [42] indicate that these conclusions remain unaltered if the linear and/or spherical contact distribution are incorporated into the simulated annealing reconstruction. It was suggested in [70] that the linear contact distribution should improve the connectivity properties of the reconstruction, but the reconstructions performed by [42] seem not to confirm this expectation.

## 6 Physical Properties

### 6.1 Exact Results

One of the main goals in studying the microstructure of porous media is to identify geometric observables that correlate strongly with macroscopic physical transport properties. To achieve this it is not only necessary to evaluate the geometric observables. One also needs to calculate the effective transport properties exactly, in order to be able to correlate them with geometrical and structural properties. Exact solutions are now becoming available and this section reviews exact results obtained recently in cooperation with J. Widjajakusuma [10,65,67]. For the disordered potential problem, specified above in equations (2) through (7), the effective macroscopic transport parameter  $\overline{C}$  is defined by

$$\langle \mathbf{j}(\mathbf{r}) \rangle = -\overline{C} \langle \nabla u(\mathbf{r}) \rangle \quad (68)$$

where the brackets denote an ensemble average over the disorder defined in (25). The value of  $\overline{C}$  can be computed numerically [33,66]. For the following results the material parameters were chosen as

$$C_{\text{P}} = 1, \quad C_{\text{M}} = 0. \quad (69)$$

Thus in the usual language of transport problems the pore space is conducting while the matrix space is chosen as nonconducting. Equations (2) through (7) need to be supplemented with boundary conditions on the surface of  $\mathbb{S}$ . A fixed potential gradient was applied between two parallel faces of the cubic sample  $\mathbb{S}$ , and no-flow boundary condition were enforced on the four remaining faces of  $\mathbb{S}$ .

The macroscopic effective transport properties are known to show strong sample to sample fluctuations. Because calculation of  $\overline{C}$  requires a disorder average the four microstructures were subdivided into eight octants of size  $128 \times 128 \times 128$ . For each octant three values of  $\overline{C}$  were obtained from the exact solution corresponding to application of the potential gradient in the  $x$ -,  $y$ - and  $z$ -direction. The values of  $\overline{C}$  obtained from dividing the measured current by the applied potential gradient were then averaged. Table 3 collects the mean and the standard deviation from these exact calculations. The standard

deviations in Table 3 show that the fluctuations in  $\overline{C}$  are indeed rather strong. If the system is ergodic then one expects that  $\overline{C}$  can also be calculated from the exact solution for the full sample. For sample EX the exact transport coefficient for the full sample is  $\overline{C}_x = 0.02046$  in the  $x$ -direction,  $\overline{C}_y = 0.02193$  in the  $y$ -direction, and  $\overline{C}_z = 0.01850$  in the  $z$ -direction [65]. All of these are seen to fall within one standard deviation of  $\overline{C}$ . The numerical values have been confirmed independently by [47].

Finally it is interesting to observe that  $\overline{C}$  seems to correlate strongly with  $p_3(L)$  shown in Fig. 11. This result emphasizes the importance of non-Hadwiger functionals because by construction there is no relationship between  $\overline{C}$  and porosity, specific surface and correlation functions.

**Table 3.** Average and standard deviation  $\sigma$  for effective macroscopic transport property  $\overline{C}$  calculated from subsamples (octants) for  $C_P = 1$  and  $C_M = 0$ .

	S <sub>EX</sub>	S <sub>DM</sub>	S <sub>GF</sub>	S <sub>SA</sub>
$\overline{C}$	0.01880	0.01959	0.00234	0.00119
$\sigma$	$\pm 0.00852$	$\pm 0.00942$	$\pm 0.00230$	$\pm 0.00234$

## 6.2 Mean Field Results

According to the general criteria discussed above in Section 3.1 a geometrical characterization of random media should be usable in approximate calculations of transport properties. In practice the full three-dimensional microstructure is usually not available in detail, and only approximate calculations can be made that are based on partial geometric knowledge.

Local porosity theory [27,28] was developed as a generalized effective medium approximation for  $\overline{C}$  that utilizes the partial geometric characterization contained in the quantities  $\mu$  and  $\lambda$ . It is therefore useful to compare the predictions from local porosity theory with those from simpler mean field approximations. The latter will be the Clausius-Mossotti approximation with  $\mathbb{P}$  as background phase

$$\begin{aligned}
 \overline{C}_c(\overline{\phi}) &= C_{\mathbb{P}} \left( 1 - \frac{1 - \overline{\phi}}{(1 - C_M/C_{\mathbb{P}})^{-1} - \overline{\phi}/3} \right) \\
 &= C_{\mathbb{P}} \left( \frac{3C_M + 2\overline{\phi}(C_{\mathbb{P}} - C_M)}{3C_{\mathbb{P}} - \overline{\phi}(C_{\mathbb{P}} - C_M)} \right), \tag{70}
 \end{aligned}$$

the Clausius-Mossotti approximation with  $\mathbb{M}$  as background phase

$$\begin{aligned} \bar{C}_b(\bar{\phi}) &= C_{\mathbb{M}} \left( 1 - \frac{\bar{\phi}}{(1 - C_{\mathbb{P}}/C_{\mathbb{M}})^{-1} - (1 - \bar{\phi})/3} \right) \\ &= C_{\mathbb{M}} \left( \frac{2C_{\mathbb{M}} + C_{\mathbb{P}} + 2\bar{\phi}(C_{\mathbb{P}} - C_{\mathbb{M}})}{2C_{\mathbb{M}} + C_{\mathbb{P}} - \bar{\phi}(C_{\mathbb{P}} - C_{\mathbb{M}})} \right), \end{aligned} \tag{71}$$

and the self-consistent effective medium approximation [35,37]

$$\bar{\phi} \frac{C_{\mathbb{P}} - \bar{C}}{C_{\mathbb{P}} + 2\bar{C}} + (1 - \bar{\phi}) \frac{C_{\mathbb{M}} - \bar{C}}{C_{\mathbb{M}} + 2\bar{C}} = 0 \tag{72}$$

which leads to a quadratic equation for  $\bar{C}$ . The subscripts  $b$  and  $c$  in (71) and (70) stand for "blocking" and "conducting". In all of these mean field approximations the porosity  $\bar{\phi}$  is the only geometric observable representing the influence of the microstructure. Thus two microstructures having the same porosity  $\bar{\phi}$  are predicted to have the same transport parameter  $\bar{C}$ . Conversely, measurement of  $\bar{C}$  combined with the knowledge of  $C_{\mathbb{M}}, C_{\mathbb{P}}$  allows to deduce the porosity from such formulae.

If the microstructure is known to be homogeneous and isotropic with bulk porosity  $\bar{\phi}$ , and if  $C_{\mathbb{P}} > C_{\mathbb{M}}$ , then the rigorous bounds [8,24,62]

$$\bar{C}_b(\bar{\phi}) \leq \bar{C} \leq \bar{C}_c(\bar{\phi}) \tag{73}$$

hold, where the upper and the lower bound are given by the Clausius-Mossotti formulae, eqs. (71) and (70). For  $C_{\mathbb{P}} < C_{\mathbb{M}}$  the bounds are reversed.

The proposed selfconsistent approximations for the effective transport coefficient of local porosity theory reads [27]

$$\int_0^1 \frac{\bar{C}_c(\phi) - \bar{C}}{\bar{C}_c(\phi) + 2\bar{C}} \lambda_3(\phi, L) \mu(\phi, L) d\phi + \int_0^1 \frac{\bar{C}_b(\phi) - \bar{C}}{\bar{C}_b(\phi) + 2\bar{C}} (1 - \lambda_3(\phi, L)) \mu(\phi, L) d\phi = 0 \tag{74}$$

where  $\bar{C}_b(\phi)$  and  $\bar{C}_c(\phi)$  are given in eqs. (71) and (70). Note that (74) is still preliminary, and a generalization is in preparation. A final form requires generalization to tensorial percolation probabilities and transport parameters. Equation (74) is a generalization of the effective medium approximation. In fact, it reduces to eq. (72) in the limit  $L \rightarrow 0$ . In the limit  $L \rightarrow \infty$  it also reduces to eq. (72) albeit with  $\bar{\phi}$  in eq. (72) replaced with  $\lambda_3(\bar{\phi})$ . In both limits the basic assumptions underlying all effective medium approaches become invalid. For small  $L$  the local geometries become strongly correlated, and this is at variance with the basic assumption of weak or no correlations. For large  $L$  on the other hand the assumption that the local geometry is sufficiently simple becomes invalid [27]. Hence one expects that formula (74) will yield good results only for intermediate  $L$ . The question which  $L$  to choose has been discussed in the literature

[3,10,12,33,66]. For the results in Table 4 the so called percolation length  $L_p$  has been used which is defined through the condition

$$\left. \frac{d^2 p_3}{dL^2} \right|_{L=L_p} = 0 \tag{75}$$

assuming that it is unique. The idea behind this definition is that at the inflection point the function  $p_3(L)$  changes most rapidly from its trivial value  $p_3(0) = \bar{\phi}$  at small  $L$  to its equally trivial value  $p_3(\infty) = 1$  at large  $L$  (assuming that the pore space percolates). The length  $L_p$  is typically larger than the correlation length calculated from  $G(r)$  [10,11].

The results obtained by the various mean field approximations are collected in Table 4 [65,67]. The exact result is obtained by averaging the three values for the full sample EX given in the previous section. The additional geometric information contained in  $\mu$  and  $\lambda$  seems to give an improved estimate for the transport coefficient.

**Table 4.** Effective macroscopic transport property  $\bar{C}$  calculated from Clausius-Mossotti approximations ( $\bar{C}_c, \bar{C}_b$ ), effective medium theory  $\bar{C}_{\text{EMA}}$  and local porosity theory  $\bar{C}_{\text{LPT}}$  compared with the exact result  $\bar{C}_{\text{exact}}$  (for  $C_P = 1$  and  $C_M = 0$ ).

$\bar{C}_c$	$\bar{C}_b$	$\bar{C}_{\text{EMA}}$	$\bar{C}_{\text{LPT}}$	$\bar{C}_{\text{exact}}$
0.094606	0.0	0.0	0.025115	0.020297

ACKNOWLEDGEMENT: Most results reviewed in this paper were obtained in cooperation with B. Biswal, C. Manwart, J. Widjajakusuma, P.E. Øren, S. Bakke, and J. Ohser. I am grateful to all of them, and to the Deutsche Forschungsgemeinschaft as well as Statoil A/S Norge for financial support.

## References

- Adler, P. (1992): *Porous Media* (Butterworth-Heinemann, Boston)
- Adler, P., C. Jacquin, C., J. Quiblier (1990): ‘Flow in simulated porous media’, *Int.J.Multiphase Flow* **16**, p. 691
- Andraud, C., A. Beghdadi, E. Haslund, R. Hilfer, J. Lafait, B. Virgin (1997): ‘Local entropy characterization of correlated random microstructures’, *Physica A* **235**, p. 307
- Bakke, S., P. Øren (1997): ‘3-d pore-scale modeling of sandstones and flow simulations in pore networks’, *SPE Journal* **2**, p. 136
- Barut, A., R. Raczka (1986): *Theory of Group Representations and Applications* (World Scientific, Singapore)
- Bear, J. (1972): *Dynamics of Fluids in Porous Media* (Elsevier Publ. Co., New York)
- Bear, J., A. Verruijt (1987): *Modeling Groundwater Flow and Pollution* (Kluwer Academic Publishers, Dordrecht)

8. Bergman, D. (1982): 'Rigorous bounds for the complex dielectric constant of a two-component composite', *Ann. Phys.* **138**, p. 78
9. Biswal, B., R. Hilfer (1999): 'Microstructure analysis of reconstructed porous media', *Physica A* **266**, p. 307
10. Biswal, B., C. Manwart, R. Hilfer, R. (1998): 'Threedimensional local porosity analysis of porous media', *Physica A* **255**, p. 221
11. Biswal, B., C. Manwart, R. Hilfer, S. Bakke, P. Øren (1999): 'Quantitative analysis of experimental and synthetic microstructures for sedimentary rock', *Physica A* **273**, p. 452
12. Boger, F., J. Feder, R. Hilfer, R., T. Jøssang (1992): 'Microstructural sensitivity of local porosity distributions', *Physica A* **187**, p. 55
13. Bourbie, T., O. Coussy, B. Zinszner (1987): *Acoustics of Porous Media* (Editions Technip, Paris)
14. Bourbie, T., B. Zinszner (1995): 'Hydraulic and acoustic properties as a function of porosity in Fontainebleau sandstone', *J. Geophys. Res.* **90**, p. 11524
15. Bryant, S., D. Mellor, D., C. Cade (1993): 'Physically representative network models of transport in porous media', *AIChE Journal* **39**, p. 387
16. Chatzis, I., F. Dullien (1977): 'Modelling pore structure by 2-d and 3-d networks with applications to sandstones', *J. of Canadian Petroleum Technology*, p. 97
17. Crivelli-Visconti, I. (ed.) (1998): *ECCM-8 European Conference on Composite Materials* (Woodhead Publishing Ltd, Cambridge)
18. Delfiner, P. (1972): 'A generalization of the concept of size', *J. Microscopy* **95**, p. 203
19. Diebels, S., W. Ehlers (1996): 'On fundamental concepts of multiphase micropolar materials', *Technische Mechanik* **16**, p. 77
20. Dullien, F. (1992): *Porous Media - Fluid Transport and Pore Structure* (Academic Press, San Diego)
21. Ehlers, W. (1995): 'Grundlegende Konzepte in der Theorie poröser Medien', Technical report, Institut f. Mechanik, Universität Stuttgart, Germany
22. Fatt, I. (1956): 'The network model of porous media I. capillary pressure characteristics', *AIME Petroleum Transactions* **207**, p. 144
23. Hadwiger, H. (1955): *Altes und Neues über konvexe Körper* (Birkhäuser, Basel)
24. Hashin, Z., S. Shtrikman (1962): 'A variational approach to the theory of effective magnetic permeability of multiphase materials', *J. Appl. Phys.* **33**, p. 3125
25. Haslund, E., B. Hansen, R. Hilfer, B. Nøst (1994): 'Measurement of local porosities and dielectric dispersion for a water saturated porous medium', *J. Appl. Phys.* **76**, p. 5473
26. Hearst, J., P. Nelson (1985): *Well Logging for Physical Properties* (McGraw-Hill, New York)
27. Hilfer, R. (1991): 'Geometric and dielectric characterization of porous media', *Phys. Rev. B* **44**, p. 60
28. Hilfer, R. (1992): 'Local porosity theory for flow in porous media', *Phys. Rev. B* **45**, p. 7115
29. Hilfer, R. (1993): 'Local porosity theory for electrical and hydrodynamical transport through porous media', *Physica A* **194**, p. 406
30. Hilfer, R. (1996): 'Transport and relaxation phenomena in porous media', *Advances in Chemical Physics* **XCII**, p. 299
31. Hilfer, R., B. Nøst, E. Haslund, Th. Kautzsch, B. Virgin, B.D. Hansen (1994): 'Local porosity theory for the frequency dependent dielectric function of porous rocks and polymer blends', *Physica A* **207**, p. 19

32. Hilfer, R., T. Rage, B. Virgin (1997): 'Local percolation probabilities for a natural sandstone', *Physica A* **241**, p. 105
33. Hilfer, R., J. Widjajakusuma, B. Biswal (1999): 'Macroscopic dielectric constant for microstructures of sedimentary rocks', *Granular Matter*, in print
34. Katz, A., A. Thompson (1986): 'Quantitative prediction of permeability in porous rock', *Phys. Rev. B* **34**, p. 8179
35. Kirkpatrick, S. (1973): 'Percolation and conduction', *Rev. Mod. Phys.* **45**, p. 574
36. Lake, L. (1989): *Enhanced Oil Recovery* (Prentice Hall, Englewood Cliffs)
37. Landauer, R. (1978): 'Electrical conductivity in inhomogeneous media', in: *Electrical Transport and Optical Properties of Inhomogeneous Materials*, ed. by J. Garland, D. Tanner (American Institute of Physics, New York), p. 2
38. Levitz, P., D. Tchoubar (1992): 'Disordered porous solids: From chord distributions to small angle scatterin', *J. Phys. I France* **2**, p. 771
39. Louis, A. (1989): *Inverse und schlecht gestellte Probleme* (Teubner, Stuttgart)
40. Manwart, C., R. Hilfer (1999a): to be published
41. Manwart, C., R. Hilfer (1999b): 'Reconstruction of random media using Monte Carlo methods', *Physical Review E* **59**, p. 5596
42. Manwart, C., S. Torquato, R. Hilfer (1999): 'Stochastic reconstruction of sandstones', preprint
43. Marsily, G. (1986): *Quantitative Hydrogeology – Groundwater Hydrology for Engineers* (Academic Press, San Diego)
44. Mecke, K. (1998): 'Integral geometry and statistical physics', *Int. J. Mod. Phys. B* **12**, p. 861
45. Mecke, K., H. Wagner (1991): 'Euler characteristic and related measures for random geometric sets', *J. Stat. Phys.* **64**, p. 843
46. Muehe, L., D. Stoyan (1992): 'Contact and chord length distributions of the poisson voronoi tessellation', *Journal of applied probability* **29**, p. 467
47. Øren, P. (1999): private communication
48. Øren, P., S. Bakke, O. Arntzen (1998): 'Extending predictive capabilities to network models', *SPE Journal*, p. SPE 38880
49. Quiblier, J. (1984): 'A new three dimensional modeling technique for studying porous media', *J. Colloid Interface Sci.* **98**, p. 84
50. Roberts, A. (1997): 'Statistical reconstruction of three-dimensional porous media from two-dimensional images', *Phys.Rev.E* **56**, p. 3203
51. Roberts, J., L. Schwartz (1985): 'Grain consolidation and electrical conductivity in porous media', *Phys. Rev. B* **31**, p. 5990
52. Roy, D. (1991): *Methods of Inverse problems in Physics* (CRC Press, Boca Raton)
53. Roy, S., S. Tarafdar, S. (1997): 'Archies's law from a fractal model for porous rock', *Phys.Rev.B* **55**, p. 8038
54. Sahimi, M. (1993): 'Flow phenomena in rocks: From continuum models to fractals, percolation, cellular automata and simulated annealing', *Rev. Mod. Phys.* **65**, p. 1393
55. Sahimi, M. (1995): *Flow and Transport in Porous Media and Fractured Rock* (VCH Verlagsgesellschaft mbH, Weinheim)
56. Scheidegger, A. (1974): *The Physics of Flow Through Porous Media* (University of Toronto Press, Toronto)
57. Schneider, R. (1993): *Convex Bodies: The Brunn-Minkowski Theory* (Cambridge University Press, Cambridge)
58. Schneider, R., W. Weil (1992): *Integralgeometrie* (Teubner, Stuttgart)
59. Schwartz, L., S. Kimminau (1987): 'Analysis of electrical conduction in the grain consolidation model', *Geophysics* **52**, p. 1402

60. Stell, G. (1985) 'Mayer-Montroll equations (and some variants) through history for fun and profit', in: *The Wonderful World of Stochastics*, ed. by M. Shlesinger, G. Weiss (Elsevier, Amsterdam), p. 127
61. Stoyan, D., W. Kendall, J. Mecke (1987): *Stochastic Geometry and its Applications* (Akademie-Verlag / Wiley, Berlin / Chichester)
62. Torquato, S. (1991): 'Random heterogeneous media: Microstructure and improved bounds on effective properties', *Applied mechanics reviews* **44**, p. 37
63. Torquato, S., G. Stell (1982): 'Microstructure of Two Phase Random Media I: The  $n$ -Point Probability Functions', *J. Chem. Phys.* **77**, p. 2071
64. Virgin, B., E. Haslund, R. Hilfer (1996): 'Rescaling relations between two- and three dimensional local porosity distributions for natural and artificial porous media', *Physica A* **232**, p. 1
65. Widjajakusuma, J., B. Biswal, R. Hilfer (1999a): 'Predicting transport parameters of heterogeneous media', preprint
66. Widjajakusuma, J., B. Biswal, R. Hilfer (1999b): 'Quantitative prediction of effective material properties of heterogeneous media', *Comp. Mat. Sci.* **16**, p. 70
67. Widjajakusuma, J., R. Hilfer (2000): 'Local Porosity Theory for Sound Propagation in Porous Media'
68. Widjajakusuma, J., C. Manwart, B. Biswal, R. Hilfer (1999): 'Exact and approximate calculations for conductivity of sandstones', *Physica A* **16**, p. 70
69. Yao, J., P. Frykman, F. Kalaydjian, P. Thovert, P. Adler (1993): 'High-order moments of the phase function for real and reconstructed model porous media: A comparison', *J. of Colloid and Interface Science* **156**, p. 478
70. Yeong, C., S. Torquato (1998): 'Reconstructing random media', *Phys.Rev. E* **57**, p. 495
71. Ziman, J. (1982): *Models of Disorder* (Cambridge University Press, Cambridge)